

The observation of Extensive Air Showers from Space

M. Pallavicini, R. Pesce, A. Petrolini and A. Thea.
Dipartimento di Fisica dell'Università di Genova and INFN,
via Dodecaneso 33, I-16146, Genova, Italy.

December 2, 2021

Abstract

We summarise some basic issues relevant to the optimisation and design of space-based experiments for the observation of the Extensive Air Showers produced by Ultra-High Energy Cosmic Particles interacting with the atmosphere. A number of basic relations is derived and discussed with a twofold goal: defining requirements for the experimental apparatus and estimating the expected performance.

Contents

1	Introduction	2
2	The observational approach	3
3	Scientific requirements	3
3.1	The experimental apparatus	5
3.2	Architecture of the instrument	5
3.2.1	Mission requirements	5
3.2.2	Requirements for the digital camera	6
4	Definitions and assumptions	6
4.1	Some geometry definitions	7
4.2	Reference conditions and general assumptions	7
4.3	The air scintillation signal	12
4.3.1	Single-photon detection factors	13
4.3.2	Multi-photon detection factors	14
5	Design and optimisation of a space-borne apparatus	14
5.1	Orbit	14
5.2	Optical system design	15
5.2.1	Entrance pupil of the optics	15
5.2.2	FoV of the optics	16
5.2.3	Reflective or refractive ?	16
5.3	Effect of the observation angle (location on the FS)	16
5.3.1	Signal and RB roll-off with field-angle	16
5.3.2	Other considerations	17
5.4	The photo-detector on the FS	17
5.4.1	The parameters of the Photo-Detector	17
5.5	Number of detected photons, efficacy and energy resolution	19
5.6	The length and duration of the visible EAS image	19
5.7	Aperture	21
5.7.1	Area observed at the Earth	21
5.7.2	Instantaneous geometrical aperture	29
5.7.3	Tilting of the apparatus	30
5.7.4	Duty cycle	31
5.8	Pixel size and angular resolution	31
5.8.1	Angular resolution perpendicular to the line of sight	32

arXiv:0810.5711v1 [astro-ph] 31 Oct 2008

5.8.2	Angular resolution parallel to the line of sight	32
5.9	X_M resolution	33
5.10	Noise and background	34
6	Some order of magnitude estimates	35
6.1	Air scintillation signal	35
6.2	Requirements on the optical triggering efficacy	35
6.3	Granularity and angular resolution	36
6.4	The random background (RB)	36
7	Conclusions	36
	Acknowledgments	37

1 Introduction

Ultra-High Energy Cosmic Particles (UHECP) with energies in excess of $\approx 10^{19}$ eV hit the Earth with a very low flux of about one particle $\cdot \text{km}^{-2} \cdot \text{sr}^{-1} \cdot \text{millennium}^{-1}$, for particles with energy $E \gtrsim 10^{20}$ eV [1].

The observation of UHECP and the interpretation of the related phenomenology is one of the most challenging topics of modern High-Energy Astro-Particle Physics. Direct detection is impossible at these energies, due to the exceedingly low flux, but UHECP can be detected by observing the Extensive Air Showers (EAS) produced by the interaction of the primary particle with the Earth atmosphere. See [2, 3, 4], and references therein, for recent reviews on these topics.

The ground-based Pierre Auger Observatory (PAO) [5] is currently taking data: its south site in Argentina and its forthcoming north site in the US will provide in the next few years, a clear understanding of many important topics [6, 1]. However it is likely that the next generation of experiments for the study of UHECP, after PAO, will be space-based, in order to increase the event statistics by exploiting the larger instantaneous geometrical aperture which can be obtained by a space observatory with respect to ground based experiments.

The aim of this paper is to discuss and summarise a few key issues relevant to the design and optimisation of space-based experiments for the observation of UHECP. Analytical and semi-analytical relations will be presented and discussed, in order to roughly set the scenario for space-based observation of EAS.

A first discussion of these arguments can be found in [7], which was a starting point for many of the results derived here.

The results we present are a basic input to the design and optimisation of the experimental apparatus. Obviously these results cannot replace a full Monte-Carlo simulation, for detailed studies. However they are exceedingly useful to improve the basic understanding, for a fast outlook and for a rough cross-check of the detailed Monte-Carlo simulation results. The basics of the optimisation of the experiment design can be easily understood using the results we will present, leaving the hard work of a full Monte-Carlo simulation to a second phase. In fact the very many important parameters affecting the performance do not allow to perform a full Monte-Carlo simulation of all the possible cases: the results presented here provide therefore valuable starting points for detailed Monte-Carlo simulations.

A full Monte-Carlo simulation was developed in the framework of the EUSO Collaboration: ESAF [8, 9], allowing to extract detailed predictions. In fact most of the work presented in this paper is the result of the development of the EUSO experiment [10], a path-finder mission of the European Space Agency (ESA), which successfully completed its phase A study in 2004 but was frozen afterwards due to programmatic and financial reasons. A large part of the scientific community is now looking forward to both the path-finder Japan-lead mission JEM-EUSO [11] and to the most challenging mission (super-EUSO [12]) in the framework of the ESA Cosmic Vision program 2015-2025 [13].

The results presented in this paper were extensively used in the concept study of the EUSO [14] and super-EUSO [12] experiments.

In fact the design of a space-based apparatus for the observation of UHECP is a very challenging task with very little design margins, as it will be clear from the results we present. It is therefore important both to optimise the design from the beginning and to set safe design margins since the beginning of the concept study itself.

2 The observational approach

John Linsley [15], in 1982, first suggested that the Earth atmosphere at night, viewed from space, constitutes a huge calorimeter for remotely observing UHECP (SOCRAS). Yoshiyuki Takahashi, together with John Linsley and Livio Scarsi, resurrected the original idea in 1995, when the concept seemed to be close to be technically feasible (Space AirWatch). Since then a number of proposals and studies were carried on, including the OWL [16] (Orbiting Wide-angle Light-collectors) project, the TUS/KLYPVE [17] project and EUSO [10]. In more recent times the JEM-EUSO [11] Collaboration aims to propose again the EUSO concept on the International Space Station while the super-EUSO proposal [12], for a most challenging next-generation experiment, has been recommended by ESA for technological developments.

A space-based experiment can detect the near-UV air scintillation light isotropically produced during the EAS development in the atmosphere by the interaction of the EAS secondary particles with the air molecules. The measurement of the scintillation light allows to record the EAS development. Additional information can be gathered by observing the Cherenkov light diffusely reflected at the Earth surface (by land, sea or clouds). The Earth atmosphere plays the role of a giant calorimeter, although it is passive, continuously changing and outside the human control.

This approach is complementary to ground-based observations. In fact EAS develop close to the Earth surface. Therefore, thanks to the large average distance from the EAS of an Earth orbiting apparatus, a large FoV apparatus can watch a huge target of atmosphere, so that the space-based observation is best suited for observing very low fluxes and/or particles weakly interacting with the atmosphere. Nevertheless, due to the larger distance from the EAS with respect to ground-based experiments, the signal is much fainter and therefore the EAS reconstruction is worse than at ground-based experiments.

The required apparatus is an Earth-watching large aperture, large FoV, fast and highly pixelised digital camera for detecting near-UV single Photo-ns superimposed on a huge background, capable of three to five years of operation in space, at least.

Any EAS is seen by the apparatus as a point moving on its Focal Surface (FS) with a direction and an angular velocity depending on the EAS primary direction with respect to the line-of-sight. These characteristics allow one to distinguish the EAS from the various types of background (see section 5.10), because, typically, those have a different space-time development.

The general scheme of the observational approach is shown in figure 1.

3 Scientific requirements

The following typical scientific requirements for UHECP observation from space are assumed for indication purposes only (see [12]). Depending on the scientific objectives different requirements might be used by adapting the relations to the case considered.

- All sky coverage.
- Spatial granularity and resolution of the EAS image projected at the Earth: $\Delta\ell \sim 0.5$ km or better, in order to ensure a good enough reconstruction of the UHECP.
- Sampling time of the EAS signal of order of $\Delta t \sim \mu\text{s}$ or better, in order to ensure a good enough reconstruction of the UHECP.
- Angular resolution on the reconstructed primary UHECP direction: $\Delta\psi \lesssim (1^\circ \div 3^\circ)$ for a large enough subsample of events, in order to allow source identification and taking into account the deviation induced by magnetic fields on charged particles.
- Energy resolution: $\Delta E/E \lesssim 0.3$.
- Resolution on the depth of the EAS maximum measurement $\Delta X_M \lesssim 50$ g/cm² (accounting for the intrinsic variability of the EAS development).
- Energy threshold: $E_{\text{TH}} \approx 1 \cdot 10^{19}$ eV, with a flat efficiency plateau at $E \gtrsim E_{\text{TH}}$ to keep systematic effects well under control. This also ensures a fair overlap with the energy spectrum observed by ground-based experiments.
- Capability to measure EAS with energies up to $E_{\text{MAX}} \approx 10^{21}$ eV.
- Instantaneous geometrical aperture, \mathcal{A}_g , one order of magnitude larger than currently existing and/or planned ground-based experiments: $\mathcal{A}_g \gtrsim 10^6$ km² · sr.

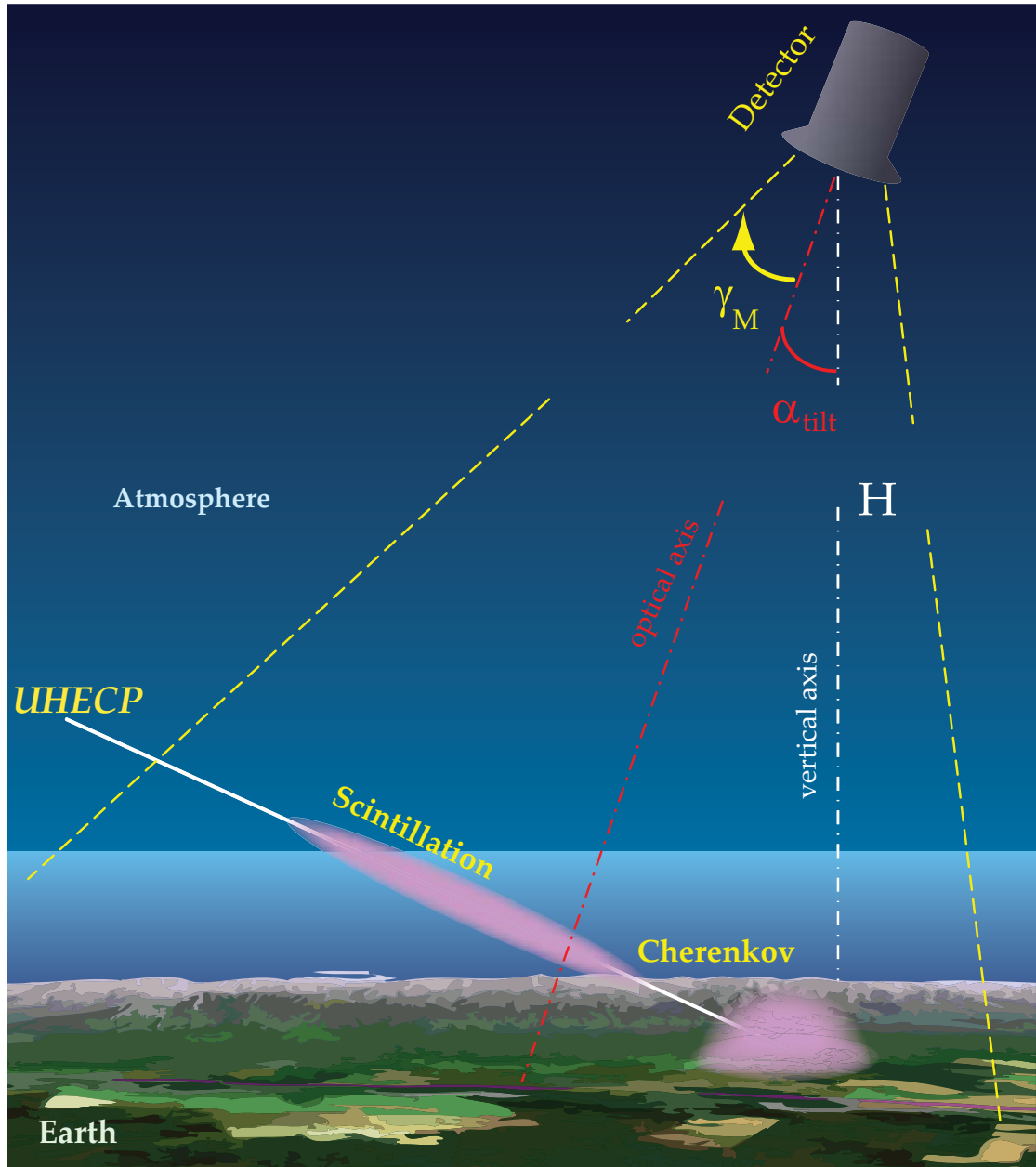


Figure 1: AirWatch observational approach: H is the orbital height, γ_M , the FoV half-angle and α_{tilt} is the tilt angle between the optical axis and the local nadir.

3.1 The experimental apparatus

The design of an apparatus for the UHECP detection from space is a very challenging task, because of the low expected rate of events, the faint signal from any EAS and the tight technical constraints (especially on mass, power, volume and telemetry) imposed on a space experiment as well as the harsh space environment.

The engineering is very complex and the design has a very strong impact on the scientific performances. A careful optimisation is therefore mandatory.

3.2 Architecture of the instrument

The required experimental apparatus is made of the following parts.

- The main digital camera, which is assumed to have cylindrical symmetry around the optical axis, operating in the near-UV, a large aperture, large FoV, fast and pixelized single Photo-n detector, consisting of:
 - the main reflective deployable optics; it consists of:
 - * the main mirror: a large, lightweight, segmented, nearly spherical, deployable mirror;
 - * the corrector plate on the entrance pupil which needs to be deployable as well;
 - * the optical filters;
 - * active control mechanism for both the mirror and the corrector plate;
 - * supporting structure.
 - The Photo-Detector (PD) on the focal surface (FS) of the optics; it consists of:
 - * a bidimensional array of sensors;
 - * the light-collection system on the sensor;
 - * the f/e electronics chip and ancillary electronics;
 - * the housing;
 - * the back-end, trigger and on-board data-handling electronics.
- The Atmospheric Monitoring System (AM), capable to monitor the relevant atmospheric properties by a suitable instrumentation.
- The Monitoring, Alignment and Self-Calibration system (MAC).
- A Radio Pulse Detection system (RPD).
- The Central Control Unit (CCU), providing the intelligence to all the systems.
- The system and other ancillary parts including:
 - the mechanical structure, including the external protection;
 - the thermal control system;
 - the power system, including solar panels and batteries;
 - the shutter;
 - the optical baffle.
- The ground-support equipment.

3.2.1 Mission requirements

The following mission requirements are envisaged.

- An accurately designed orbit (see 5.1). The ground-track of the satellite orbit needs to be optimized according to the following parameters: minimization of natural and man-made light entering the FoV (Sun, Moon and any other light source); maximization of the rate of passages above a few fixed points at the Earth surface, for both exploiting ground calibration sources and hybrid observations and cross-calibrations with ground-based experiments. A free-flyer can give many degrees of freedom in the choice of an optimized orbit and the orbit strongly affects both the performance and the operations. A careful orbit optimization is a complex task requiring a full phase-A study. However it is not considered to be a critical issue at this stage as the orbital parameters can be varied to a large extent.

- Observation of a mass of atmosphere as large as possible, attaining a good enough geometrical acceptance which implies a large enough FoV.
- No FoV obstruction and no parasitic lights coming from any other spatial device nor from the Earth.
- Dimensions after deploying shall be dictated by the optics, including the optical baffle and the optical shutter.
- Light-tightness: the interior of the instrument shall be light tight such that the parasitic lights impinging onto the Photo-Detector will be two orders of magnitude less than the expected night-glow background rate in order not to spoil the energy resolution.
- Thermal control shall be provided to stabilize the large surfaces of the instrument with large power consumption.
- Electrical requirements: the scientific operations will have a low duty cycle. It is envisaged that during 2/3 of the orbit the Instrument will be in a standby status of low-power consumption. The power consumption quoted for operations is thus required during roughly 1/3 of the orbit only.
- Attitude: approximate nadir pointing; pointing accuracy is not a critical factor provided the absolute direction of the instrument axis is known/measured for off-line use. It is assumed nadir pointing to within a few degrees with pointing direction known offline to within $\Delta\chi \simeq 0.5^\circ$, well below the expected angular resolution of the instrument.
- Telemetry and telecommanding: the expected event rate will be high and it will depend on the final orbit, affecting the event rates. A precise estimation is currently lacking.
- Required lifetime: five years minimum, ten years goal.

3.2.2 Requirements for the digital camera

The basic requirements for the apparatus follow.

- Single Photo-n detection in the wavelength range $WR \equiv \{330 \text{ nm} \div 400 \text{ nm}\}$ to detect the air scintillation signal. Shorter wavelengths suffer absorption from the ozone layer.
- The faintness of the signal requires high photon collection capabilities and photon detection efficiency, as well as low noise (both intrinsic and externally generated). Small cross-talk and after-pulse rates are required to keep a good enough energy resolution.
- A dynamic range spanning some three orders of magnitudes in the EAS energy, that is in the signal, in order to cover the range from the required threshold energy up to E_{MAX} .
- An efficient and selective trigger system, to achieve a good background rejection on-board, and a powerful on-board data handling system.
- Complete modularity of the apparatus to reduce the risk of single point failures.
- Compatibility with the constraints relevant to a space mission including mass, power, volume, telemetry, as well as the many environmental factors.

4 Definitions and assumptions

We will use some simplifying assumptions in order to deduce the basic relations and use analytical or semi-analytical relations whenever possible.

4.1 Some geometry definitions

The EAS properties depend, to a first approximation, on the primary particle identity, on its energy E and zenith angle, θ . The features of the EAS image also depend on the location of the EAS image inside the FoV of the apparatus, as defined by the field-angle γ of a specific point of the EAS image, and the azimuth angle of the EAS image projected at the Earth surface.

The angle between the latter and the radial direction in the FoV is called ψ_a . Let the EAS direction azimuth angle, with respect to a global reference system $Oxyz$, be φ and the azimuth angle of the line of sight in the FoV be ϕ . Clearly $\psi_a = \varphi - \phi$ (figure 2). The unit vectors of the EAS direction \hat{n} and of the line of sight \hat{s} in the frame $Oxyz$ are respectively

$$\begin{aligned}\hat{n} &= \{-\sin \theta \cos \varphi, -\sin \theta \sin \varphi, -\cos \theta\} \quad , \\ \hat{s} &= \{\sin \gamma \cos \phi, \sin \gamma \sin \phi, -\cos \gamma\} \quad .\end{aligned}$$

For an apparatus with cylindrical symmetry, there is no dependence on ϕ , but only on ψ_a .

Let β be the angle between the EAS direction and line of sight \hat{s} from the apparatus to the actual EAS location:

$$\cos(\beta) = \cos(\gamma) \cos(\theta) - \cos(\psi_a) \sin(\gamma) \sin(\theta) \quad . \quad (1)$$

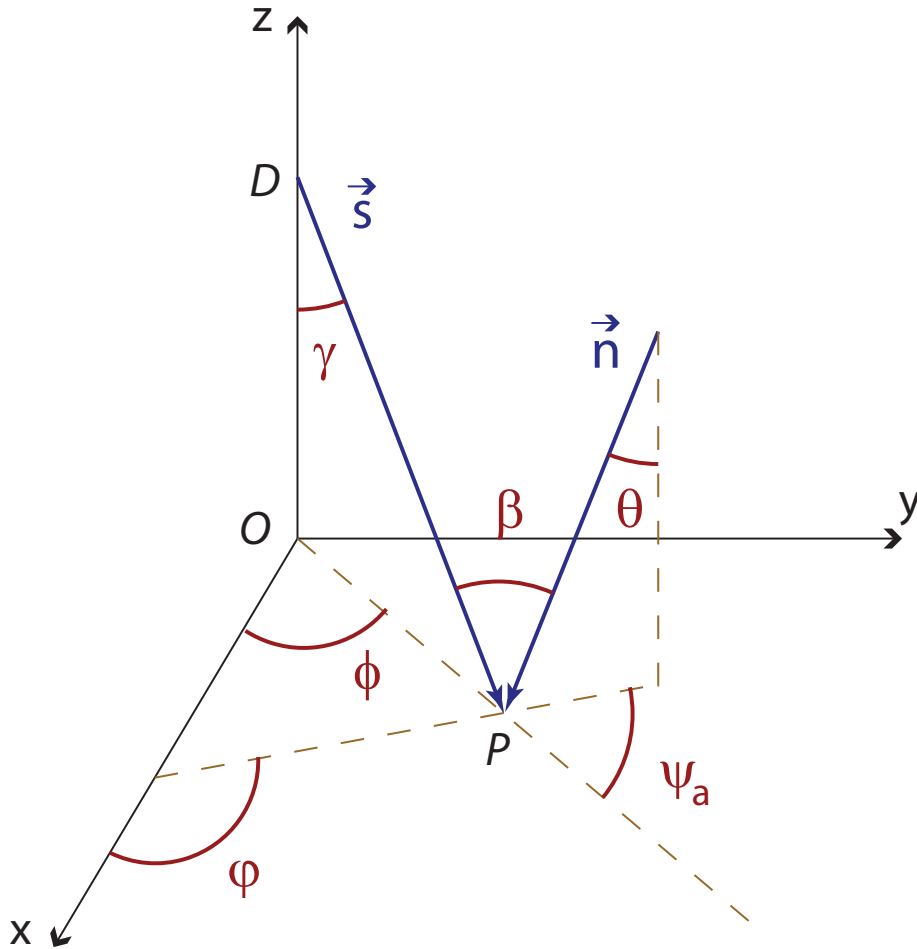


Figure 2: Definition of the angles in the FoV with respect to a global reference frame $Oxyz$. The point D is the detector position while the point P is the impact point on the EAS on the Earth surface.

4.2 Reference conditions and general assumptions

In this paper, unless otherwise specified, we shall use, as a reference, the conditions and parameters summarised in table 1.

Quantity	Reference value	Other values
Energy	$E = 10^{19}$ eV	
Zenith angle	$\theta = 50^\circ$	$\theta = 30^\circ, 70^\circ$
Azimuth angle	$\psi_a = 90^\circ$	$\psi_a = 0^\circ, 180^\circ$
Orbital height of the detector	$H = 700$ km	$H = (400 \div 1000)$ km
FoV aperture (half-angle)	$\gamma_M = 20^\circ$	$\gamma_M = 15^\circ, 25^\circ$
Field Angle of observation ^a	$\gamma = 15^\circ$	$\gamma = 10^\circ, 20^\circ$
Tilt angle of the detector	$\alpha_{\text{tilt}} = 0^\circ$	
Total photo-detection efficiency	$\epsilon_{\text{PD}} = 0.1$	
Operating Wavelength Range (WR)	$330 \text{ nm} \leq \lambda \leq 400 \text{ nm}$	
Average atmospheric transmission (in WR)	$K_{\text{atm}} \gtrsim 0.4$	
Random Background in WR [$\text{ph} \cdot \text{m}^{-2}\text{s}^{-1}\text{sr}^{-1}$]	$B = 5 \cdot 10^{11}$	$B = (0.3 \div 1.0) \cdot 10^{12}$

Table 1: The parameters and conditions used as reference in this chapter.

^aThe field angle γ is chosen approximatively at half of the FoV.

The basic parameters affecting the EAS reconstruction are: the energy, nature and direction of the EAS, the angle between the EAS direction and the line-of-sight from the apparatus to the EAS, β , the field angle of the EAS image, γ , and the altitude of the apparatus above the Earth, H .

Moreover the following general assumptions will be used in all the paper.

1. The EAS energy is fixed by the scientific requirements to have a good superposition with the spectrum observed by ground-based experiments. Therefore a reference energy $E_{\text{ref}} \approx 1 \cdot 10^{19}$ eV is used.

The EAS direction and ψ_a strongly affect the kinematics of the EAS image signal and therefore its observability and observed features. We will consider EAS with $\theta \approx 45^\circ$, which grants a good extension of the EAS with a negligible shortening of the longitudinal profile due to the impact with ground. In order to describe an average behaviour an angle $\psi_a = \pm 90^\circ$ will be used as a reference (see section 5.6).

2. The discussion will be based on typical hadron-induced EAS, with energy $E \approx (0.1 \div 10) \cdot 10^{20}$ eV and a simple apparatus, looking downward the Earth, whose configuration and characteristics will be defined during the discussion.

3. The EAS is geometrically modeled as a point moving on a straight line at the speed of light, as, basically, any EAS is seen from any realistic space-detector as a unidimensional object, on all practical purposes. A reference EAS energy $E_{\text{ref}} \approx 1 \cdot 10^{19}$ eV is used.

For several reasons, to be discussed later, we only consider EAS with a zenith angle $30^\circ \lesssim \theta \lesssim 70^\circ$. A very inclined EAS requires in any case a different treatment than an almost vertical EAS.

One should note that when observing from space the case might arise of up-going EAS, that is EAS with zenith angle larger than 90° .

4. Exponential density profile of the Earth atmosphere (assuming an isothermal atmosphere) as a function of the height, h , above the sea level [18]:

$$\rho(h) = \rho_0 \exp\left[-\frac{h}{h_0}\right] \quad \text{with} \quad \rho_0 = 1.2249 \text{ kg/m}^3 \quad \text{and} \quad h_0 = 8.4 \text{ km} \quad . \quad (2)$$

In some calculations we have also used, as a cross-check, the Linsley's parametrisation of the US Standard Atmosphere [19, 20].

5. The flat Earth approximation is used whenever applicable, that is when horizontal distances are negligible with respect to the Earth radius. When this approximation is not good enough a spherical Earth with radius $R_\oplus = 6371$ km will be used.

The flat Earth approximation does not substantially affect the results on the EAS development for zenith angle $\theta \lesssim 70^\circ$. In fact, for $\theta = 70^\circ$, the difference between the exact and the approximated value of the EAS slant depth at ground is about ~ 30 g/cm², as shown in figure 3, which is smaller than the desired resolution on the depth of the EAS maximum: ΔX_M .

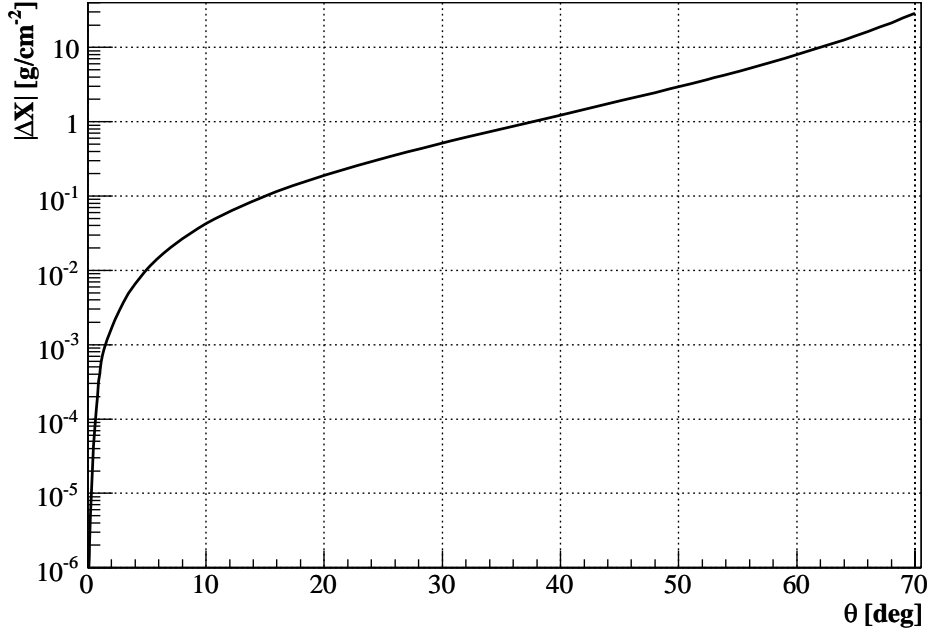


Figure 3: Absolute value of the difference $|\Delta X|$ between the true slant depth at ground and the one in flat Earth approximation versus the zenith angle.

Therefore the following approximate relation between the quota above the Earth surface, h , and the distance ℓ measured along a straight line with zenith angle θ will be assumed:

$$\frac{d\ell}{dh} = \frac{1}{\cos \theta} \quad . \quad (3)$$

The exact relation for a spherical Earth, in terms of the Earth radius R_{\oplus} , is:

$$\frac{d\ell}{dh} = \frac{h + R_{\oplus}}{\sqrt{h^2 + 2R_{\oplus}h + R_{\oplus}^2 \cos^2 \theta}} \approx \left(1 - \frac{h}{R_{\oplus}} \tan^2 \theta\right) \sec \theta \quad , \quad (4)$$

clearly showing the condition allowing to neglect the sphericity of the Earth: $\ell, h \ll R_{\oplus}$.

It is also worth remembering, for future uses, the definition of X (the so called grammage): $\frac{dX}{d\ell} = \rho$, plus the appropriate boundary condition on X at some ℓ .

6. The Gaisser-Hillas (GH) parametrisation [21, 22] of hadron-induced EAS parameterises the EAS longitudinal profile as a gamma function:

$$\begin{aligned} N(X) &= N_0 \left(\frac{X - X_0}{X_M - X_0} \right)^{(X_M - X_0)/\lambda} \exp[(X_M - X)/\lambda] \\ &= N_0 \left(\frac{X - X_0}{X_R} \right)^{X_R/\lambda} \exp[(X_R + X_0 - X)/\lambda] \quad , \quad (5) \\ &\text{for } X \geq X_0 \end{aligned}$$

where $N(X)$, the number of charged particles at the slant depth X , is expressed in terms of N_0 , the number of charged particles at the EAS maximum, X_M , the depth of the EAS maximum, X_0 , the starting point of the EAS development, $X_R \equiv X_M - X_0$ and the parameter $\lambda \simeq 65 \text{ g/cm}^2$. The second expression is used to make explicit the invariance of the EAS longitudinal profile with respect to shifts of the first interaction point X_0 .

The *pseudo-age* of an EAS at point X , is defined, closely following the age definition for an electromagnetic shower, as

$$s(X) \equiv \frac{3(X - X_0)}{(X - X_0) + 2(X_M - X_0)} \quad , \quad (6)$$

in terms of the actual slant depth and the slant depth, X_0 , of the first interaction point.

In our calculations (see [22]) X_0 can be fixed at the first interaction point and the λ parameter is rather energy independent and very similar for both proton and iron induced EAS in the energy range we are studying. Moreover $N_0 = \alpha E$ with $\alpha \simeq 0.6/\text{GeV}$ [23]. We can also roughly assume that for a primary proton EAS $X_0 \approx 35 \text{ g/cm}^2$ and for a primary iron EAS $X_0 \approx 10 \text{ g/cm}^2$ with no significant dependence on the energy.

In practice the parameter X_0 poorly correlates with the actual first interaction point, X_1 . Fixing $X_0 = X_1$ when fitting the EAS profile with the GH parametrization, produces a worse fit with X_M reduced by about 10 g/cm^2 .

Typical values for the EAS parameters, as taken from [22], are summarised in table 2. The values of X_M are the average value for different interaction models (MOCCA-Internal, MOCCA-SIBYLL, CORSIKA-SYBILL and CORSIKA-QGSJET). Note that these values are affected by X_0 when using the parametrisation of equation (5). See [22] for details.

Particle	Energy [eV]	X_M [g/cm ²]	Particle	Energy [eV]	X_M [g/cm ²]
Proton	$1.0 \cdot 10^{19}$	824 ± 55	Iron	$1.0 \cdot 10^{19}$	724 ± 20
Proton	$5.0 \cdot 10^{19}$	853 ± 58	Iron	$5.0 \cdot 10^{19}$	754 ± 20
Proton	$1.0 \cdot 10^{20}$	880 ± 54	Iron	$1.0 \cdot 10^{20}$	784 ± 19
Proton	$5.0 \cdot 10^{20}$	907 ± 49	Iron	$5.0 \cdot 10^{20}$	814 ± 19

Table 2: Typical values of EAS parameters from [22].

The height h_M of the EAS maximum as a function of the EAS zenith angle θ is shown in figure 4 for three different values of X_M using Linsley's parametrisation of the atmosphere density profile. The exponential profile for $X_M = 900 \text{ g/cm}^2$ is also shown for the sake of comparison: it is clear that the choice of the atmosphere density profile does not strongly affect h_M up to $\theta \approx (60^\circ \div 70^\circ)$.

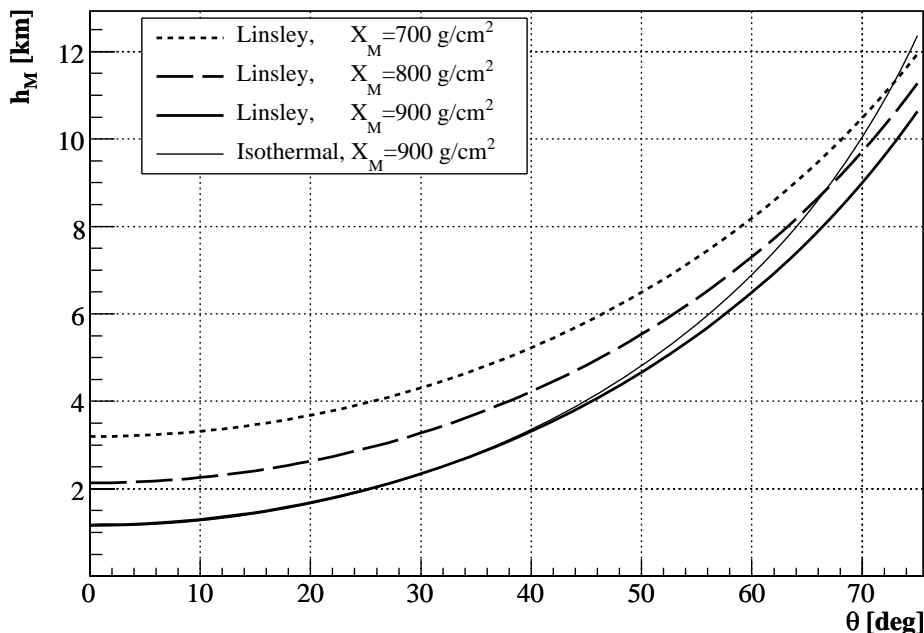


Figure 4: The height of the EAS maximum versus the EAS zenith angle.

The lateral EAS profile is not accounted for, as it is hardly accessible when observing from space.

7. A typical hadron-induced EAS of $E = (0.1 \div 10) \cdot 10^{20}$ eV with $\theta \lesssim 70^\circ$ is seen on the FS of an orbiting apparatus as a track not longer than a few degrees, as discussed in detail in section 5.6. Actually this depends on the instantaneous height of the satellite from ground: a few degrees length must be considered an upper limit, as it is calculated for $H \approx 300$ km, which is a very small orbital height for any satellite requiring a reasonably long lifetime ¹.

We can therefore neglect any possible change of the apparatus properties as a function of the field-angle for any given EAS, even if we are dealing with a large FoV optics. Obviously this would not be true for a very inclined EAS, which can appear many degrees long and cannot be easily described in a simple parameterised form.

8. The EAS develops in the atmosphere at an height $h \lesssim 20$ km. In this part of atmosphere the scintillation yield in the wavelength range WR can be considered as nearly constant [24]. Roughly $Y \simeq (4.2 \pm 0.2)$ photons particle⁻¹ m⁻¹. When a better precision is required one can use the yield measurements of [25].
9. The random background (RB) is assumed to be uniform, isotropic and constant on the space-time scale of the EAS development. We assume for the RB in the wavelength range WR a reference value: $B \approx 0.5_{-0.2}^{+0.5} \cdot 10^{12}$ photons · m⁻² · s⁻¹ · sr⁻¹.

From the current measurements we already know that, under some circumstances, it can be up to a factor two larger depending on the conditions (including moon phases and cloudiness).

It is assumed that, by continuously measuring the background nearby the EAS, both in space and in time, the underlying RB can be subtracted away, in real time. Due to the large RB this is an essential assumption in order to extract the faint EAS signal from the background at energies near E_{TH} .

The possibility to subtract the background in real-time is justified by the rather large expected RB rate, such that the relative error on the background estimate is small (see section 6.4). Therefore an appropriate statistical estimator used to compare the signal to background is S/\sqrt{B} .

10. Atmospheric transmission is naively modeled taking only into account Rayleigh scattering. In fact Mie scattering is only important at low altitudes of a few km, while the EAS predominantly develops above a few km height (see figure 4). Mie scattering is therefore ignored at the current level of approximation. Another factor which might turn out to be important is multiple scattering of the signal, which is however difficult to study without a full Monte-Carlo simulation.

A most important issue is the atmospheric transmission as a function of the zenith angle direction. Table 3 shows the ratio, r , between the atmospheric transmission from ground to infinity at a zenith angle θ and the same quantity in the vertical direction, all quantities being evaluated in the flat Earth approximation. The table shows that at $\theta \approx 75^\circ$ the atmospheric transmission is reduced by one order of magnitude with respect to the vertical transmission. This fact is a crucial one in the evaluation of the effectiveness of a tilting of the apparatus with respect to the nadir direction, as it will be discussed later.

11. The atmospheric geodesic refraction is normally negligible. Indeed, according to [18], the correction for the refraction when observing an object at the Earth surface from an height H , at a zenith angle χ with respect to the nadir, is $\Delta\chi \approx 62.37'' \tan \chi$, for $\chi \lesssim 80^\circ$ at a wavelength $\lambda = 337$ nm.

So we have $\Delta\chi \approx 0.008^\circ$ at $\chi = 25^\circ$, that is about the maximum field-angle in the case of no tilting of the detector optical axis with respect to the nadir. The effect of the refraction is small with respect to the pixel size (typically of $\sim 0.1^\circ$) and it can be neglected.

However the effect of atmospheric refraction can be huge with a tilted apparatus, when observing at large angles with respect to nadir.

12. Clear sky conditions are assumed. In fact a study taking into account all the many effects of clouds requires without any doubt a detailed Monte-Carlo simulation. Therefore we will find best-possible results.
13. Basic parameters of the apparatus are its altitude above the Earth, H , (or, in more general terms, the orbital parameters) and the tilt angle α_{tilt} between the optical axis and the local vertical.

¹This angle, as an upper limit, is easily estimated computing the EAS length between the first interaction point and the ground. The real angle seen by the detector is smaller due to the background predominance with respect to the signal at the beginning of the EAS.

χ	$\mathcal{R} \equiv \frac{\tau_a[\chi,0]}{\tau_a[\chi=0,0]}$	χ	$\mathcal{R} \equiv \frac{\tau_a[\chi,0]}{\tau_a[\chi=0,0]}$
0°	1.000	45°	0.748
5°	0.997	50°	0.678
10°	0.989	55°	0.594
15°	0.976	60°	0.497
20°	0.956	65°	0.384
25°	0.930	70°	0.260
30°	0.897	75°	0.135
35°	0.857	80°	0.036
40°	0.808	85°	$7 \cdot 10^{-4}$

Table 3: Ratio \mathcal{R} between the atmospheric transmission from ground to infinity at a zenith angle χ and the same quantity at $\chi = 0^\circ$, all quantities being evaluated in the flat Earth approximation (for a wavelength $\lambda = 337$ nm) using equation (7).

The choice of the orbit height of the apparatus requires a trade-off taking into account the low signal produced by the lower energy EAS and the requirement to observe a target of atmosphere as large as possible. Moreover practical and technical constraints may limit the orbit height.

The orbit height of the apparatus, H , is assumed to be: $300 \text{ km} \lesssim H \lesssim 1000 \text{ km}$ (see section 5.1). In fact orbits lower than about 300 km suffer too much drag and require therefore frequent reboots. Orbits higher than about 1000 km are disfavoured by the fact that the radiation environment undergoes a substantial change at about 1000 km height with the inset of Van Allen belts, whose high level of trapped radiation may greatly influence the spacecraft. Moreover orbits higher than about 1000 km turn out to provide too high a threshold for any reasonably-sized apparatus.

The orbit parameters must be tuned to optimize the expected results: energy range and instantaneous geometrical aperture can be tuned but constraints have to be taken into account.

Some of the above assumptions are optimistic with respect to the real conditions of the experiment (the clear sky assumption, for instance). This means that the results we will obtain are necessary, but possibly not sufficient, requirements for observations.

4.3 The air scintillation signal

It is worthwhile to recall the expressions giving the air scintillation signal from the EAS. Any wavelength dependence is implicit in all the following formulas.

Let w be a linear position coordinate along the EAS development ($\Delta w = c \Delta t$), let $\mathbf{x}[w] = \mathbf{x}[w[t]]$ be the current EAS position and \mathbf{y} be the current position of the observational apparatus, let $Y_e(\mathbf{x}[w]) = Y_e(\mathbf{x}[w[t]])$ be the air scintillation yield in the desired wavelength range at the EAS position, let $N_c(\mathbf{x}[w]) = N_c(\mathbf{x}[w[t]])$ be the number of charged particles in the EAS at w and let A be the entrance pupil area of the optics (which is actually the cross-section for a photon hitting the FS when $\gamma = 0$).

Let the atmospheric transmission from the generation point to the observation point be $T_A[\mathbf{x}, \mathbf{y}]$. The atmospheric absorption due to Rayleigh scattering only can be roughly parameterized as:

$$T_A[\mathbf{x}[w], \mathbf{y}] \equiv \tau_a[\chi, z] \simeq \exp \left[- \left(\frac{\rho_0 h_0}{\Lambda(\lambda)} \right) M(\chi) \exp \left(- \frac{z}{h_0} \right) \right] \quad (7)$$

$$\text{with } \frac{\rho_0 h_0}{\Lambda} \approx 0.7 \quad \text{for } \lambda = 337 \text{ nm} \quad , \quad (8)$$

where $h_0 \approx 8.4$ km is the atmosphere scale height at the sea level (see the (2)), $\rho_0 = 1.292 \text{ kg} \cdot \text{m}^{-3}$ is the atmospheric density at the sea level, z is the altitude of the photons emission point, $\Lambda(\lambda)$ is the Rayleigh mean free path at the wavelength λ (see [26]) and $M(\chi)$ is the airmass function at the zenith angle χ . For $\chi \lesssim 80^\circ$, $M(\chi) \approx \sec \chi$, a better approximation can be found for example in [27].

Let the overall detection efficiency of the PD, including the f/e electronics efficiency, be $\varepsilon_{\text{PD}}[\gamma, \mathcal{X}]$; it is the probability that a photon reaching the PD will fire the f/e electronics producing a recorded photon hit. It might depend on many parameters, \mathcal{X} , and it depends on the field-angle γ , in particular. In fact at different field-angles

the incidence angles of the incoming photons may change leading, for instance, to a change in the intrinsic sensor detection efficiency.

Let the total efficacy² [28] of the optical apparatus be $(A\varepsilon_O[\gamma])$ and the total throughput efficiency³ [28] be $\varepsilon_O[\gamma]$. The previous definitions refer to all the photons reaching any point on the FS and do not include the filter transmission, $\eta_F[\gamma]$, which is intentionally kept as a separate parameter as the filter transmission is one the the key parameters to play with.

In order to quantify the detectable signal one should build more appropriate quantities than the total efficacy and total throughput efficiency. In fact for any given direction, at an angle γ with respect to the optical axis, only the photons reaching the FS close enough to the centroid of the distribution of all the photons focused on the FS are useful for the EAS reconstruction. In fact photons too far from the centroid will contribute to the veiling glare, that is diffused background on the FS. This effect might be particularly dangerous because, thanks to the large FoV, it is most likely that bright sources are present somewhere in the FoV: in case of a large veiling glare these bright sources might significantly increase the background level on the whole FS.

A suitable fiducial region (called Ω), around the centroid of the distribution on the FS of all the photons, must be defined. The fiducial region Ω may be defined in different ways. The photons on the FS will then be classified into three classes, as follows: inside the fiducial region Ω (transmitted photons); outside the fiducial region Ω but detected somewhere on the FS (photons giving rise to the veiling glare); any other photon (lost or absorbed somewhere). It is appropriate to adopt as a fiducial region a region of the order of the spot-size and/or pixel size.

Let $\varepsilon_B[\gamma]$ be the fraction, out of all the photons on the FS, falling inside the desired bucket size: this is actually a measure of the encircled energy fraction.

Define then the *triggering efficacy* as $A\varepsilon_O[\gamma]\varepsilon_B[\gamma] \equiv A\varepsilon'_O[\gamma]$ and the *triggering throughput efficiency* as $\varepsilon_O[\gamma]\varepsilon_B[\gamma] \equiv \varepsilon'_O[\gamma]$.

Let $\Delta S[w]_{\Omega}$ (with the subscript Ω) remind that the detected signal depends on the region Ω on the FS around the the centroid of the spot (bucket) where photons are considered to be detected photons instead of background. The photons outside Ω just contribute to the veiling glare.

The number of signal photons produced by a segment Δw of the EAS, at coordinate w , and detected by the apparatus is thus:

$$\Delta S[w]_{\Omega} = \left(\frac{Y_e[\mathbf{x}[w]]N_c[\mathbf{x}[w]]\Delta w}{4\pi(\mathbf{x}[w] - \mathbf{y})^2} \right) T_A[\mathbf{x}, \mathbf{y}] (A\varepsilon_O[\gamma]) \varepsilon_B[\gamma] \eta_F[\gamma] \varepsilon_{PD}[\gamma, \mathcal{X}] \quad . \quad (9)$$

$\Delta S[w]_{\Omega}$ with the subscript Ω is meant to remind that those equations are only meaningful after specification of the region Ω on the FS over which photons are considered to be detected photons, that is photons that are close enough to the centroid of the image spot.

It is worth noting that when looking at faint signals (a few photons per pixel) the errors in formula 9 will be typically dominated by the Poisson statistical fluctuations, at least for the faintest EAS. In fact it will be shown in section 6.3 that for the faintest EAS, with a number of detected photons $N \approx 100$, one has less than ten photons per pixel with a relative statistical error of the order of 0.3, larger than the expected systematic errors ($\sim 15\%$).⁴

Using the simplifying assumptions listed in section 4 it is easy to build a parameterised semi-analytical description of the relation 9, which will be used in the rest of the paper (cfr [29, 30]):

$$\Delta S[w]_{\Omega} \simeq \frac{A_{EP}N_c\varepsilon_T}{4\pi D^2} \exp\left[-\frac{D}{D_0}\right] Y \Delta w \quad , \quad (10)$$

where ε_T is the total efficiency (optics plus photo-detector and filter), D the distance from the detector to the fluorescence emission point (it can be assumed as a constant) and $D_0 \approx 12$ km is the extinction length of light due to the atmospheric scattering (at $\lambda = 337$ nm).

4.3.1 Single-photon detection factors

The atmospheric transmission $T_A[\mathbf{x}[w], \mathbf{y}]$ is the first basic single photon detection factor. It is out of control but the experiment design should be optimised to minimise its effects.

²It is defined as the ratio the number of photons incident on the entrance pupil per time unit with an angle γ and the photon irradiance [$\text{ph}\cdot\text{m}^{-2}\text{s}^{-1}$].

³It is defined as the ratio the number of photons incident on the entrance pupil per time unit with an angle γ and the total photon flux collected by the pupil (that is given by the photon irradiance times the entrance pupil area).

⁴Obviously when fitting the profile with a given functional dependence the resulting error will be reduced by the fitting procedure.

The photon collecting power of the optics is: $A\varepsilon_O[\gamma]\varepsilon_B[\gamma]\eta_F[\gamma]$, including the effect of PSF and filters. It gives the conversion from the incoming number of photons per squared meter, at an angle γ with the optical axis, to the number of photons reaching the FS inside the region Ω . It is the quality factor for the optics as far as the number of collected photons is concerned. It is the basic and unique sizable parameter to define the optics photon collecting power.

The overall detection efficiency of the PD, $\varepsilon_{PD}[\gamma, \mathcal{X}]$, is another basic parameter which depends on a large number of factors. These factors are often very close to one but, when multiplying a large number of them, the final result may significantly depart from one. The Photon-Detection-Efficiency of the sensor is the most significant parameter which is typically much smaller than one. For standard PMT, which have already been tested in the space environment and proved suitable for applications in space, $\varepsilon_{PD} = 0.12 \div 0.15$. Recently several new high quantum efficiency photo-detectors became available on the market: GaAsP *Hybrid PhotoDiodes* (HPD) [31] and Geiger-Avalanche Photo-Diode (GAPD) [32, 33]. These devices, exploiting the intrinsic quantum efficiency of the solid state device, aim to reach a $\varepsilon_{PD} = 0.4 \div 0.6$.

The overall capability to detect photons of the instrumental apparatus can be expressed through the *photo-detection efficacy*, defined as

$$\mathcal{E}_{PD} = A \cdot \varepsilon'_O[\gamma] \cdot \eta_F[\gamma] \cdot \varepsilon_{PD}[\gamma] \quad . \quad (11)$$

4.3.2 Multi-photon detection factors

Other more complex factors will affect the EAS detection, involving multi-photon correlations and correlations between neighbouring pixels, such as: the read-out electronics and trigger efficiency, ε_{TRI} , and the analysis and event reconstruction efficiency, ε_{ANA} . These effects are very difficult to estimate without a full Monte-Carlo simulation [8, 9, 34, 35], as they depend on the contribution by all the photons at once.

Therefore naive expectations coming from single photons studies can be far too optimistic: once more simple estimates may turn out to be optimistic.

5 Design and optimisation of a space-borne apparatus

5.1 Orbit

The orbit parameters can be tuned to optimise the expected performances, in particular the energy range and the instantaneous geometrical aperture.

The orbital height (semi-major axis of the ellipse) is one of the most important parameters. In fact an higher altitude implies a larger mass of observed target atmosphere (and therefore a better instantaneous geometrical aperture) but also an higher energy threshold because of the smaller EAS signal.

Varying the orbital height is useful in order to span a larger range of energies: with an elliptic orbit the satellite spends more time at a higher altitude, gaining in effective aperture, but it also spends some time at a lower altitude, decreasing the energy threshold, where a long measuring time might be not necessary.

An orbit height spanning the range $400 \text{ km} \approx H_{MIN} \lesssim H \lesssim H_{MAX} \approx 1000 \text{ km}$, for instance, would give the capability to extend the energy range, with respect to a fixed height, by taking data at different heights, that is shifting up and down the UHECP energy range with a scaling factor: $(H_{MAX}/H_{MIN})^2 \approx 6$. Moreover the instantaneous geometrical aperture at apogee would be the same factor larger than at the perigee. On the positive side one should note that the angular granularity, at fixed ΔL , scales as H^{-1} , and not as H^{-2} .

Another way to vary the height might be to use different almost circular orbits during the mission lifetime (for example part of the time at a lower altitude and part of the time at an higher altitude). Natural orbit decay might be exploited as well.

One should remember that the orbit lifetime depends on the height and it strongly depends on the epoch of the Solar cycle (that is on the epoch of the Mission), which affects the atmospheric density.

Another key point to keep in mind is that the ballistic coefficient of the satellite is expected to be rather low, due to the large expected area-to-mass ratio. Therefore, very roughly, the orbit lifetime⁵ is expected to be of the order of a few days for $H \approx 300 \text{ km}$, a few weeks for $H \approx 400 \text{ km}$ and some years at $H \approx 700 \text{ km}$ (see figure 5).

The orbit inclination should be chosen in order to span as much as possible the Earth surface in order to obtain a sky coverage as uniform as possible.

An important parameter that depends on the orbit is the duty cycle, that should be as large as possible. For this purpose, the orbit design must be further optimised in order to avoid as much as possible the light pollution

⁵Formula and data for calculation can be found in [36].

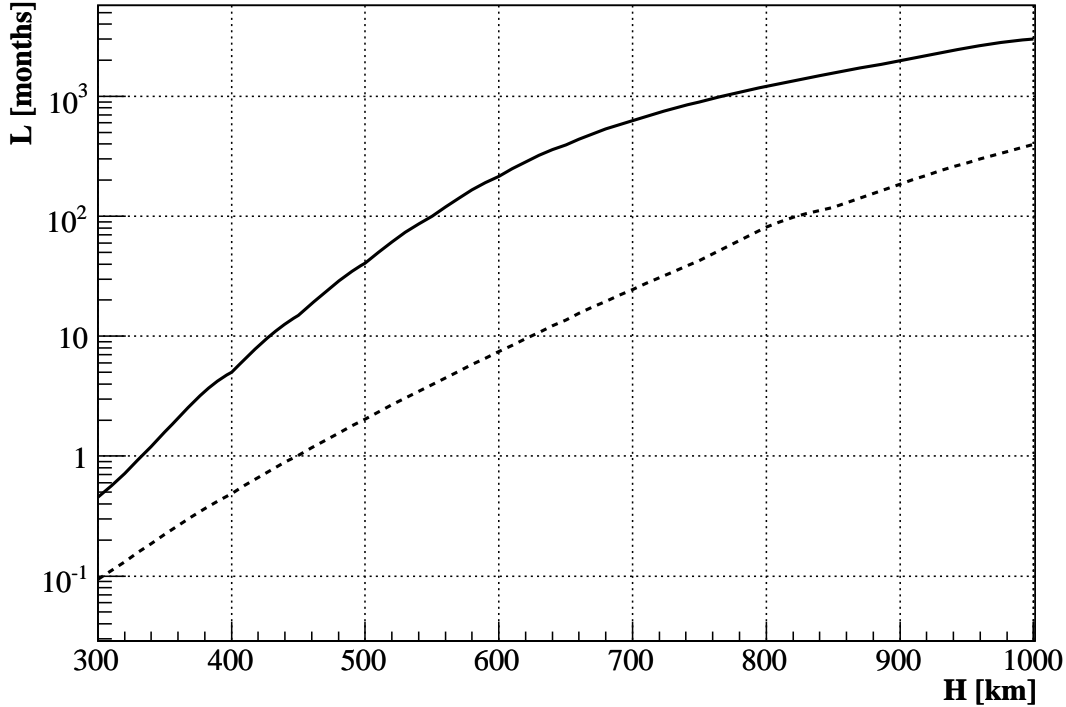


Figure 5: Lifetime L (in months) of a satellite (mass ~ 3000 kg; total area ~ 150 m²) versus the orbital height H . Solid line: solar cycle minimum; dotted line: solar cycle maximum.

from the man-made sources at ground and from the lightings (that are concentrated mainly on lands) and the auroras.

Note also that the effects of a short duty cycle can be recovered increasing the mission lifetime.

The orbit design can be also optimised in order to access as much time as possible over fixed targets at ground (ground EAS experiments, weather stations, ground-based calibration sources, etc.). In particular, the accesses to other EAS experiments, namely the Pierre Auger Observatory, are very useful for the apparatus calibration.

5.2 Optical system design

The two basic optical parameters, affecting both the performance and the engineering of the experiment, are the Entrance Pupil (EP) area, A_{EP} , and the Field of View (FoV) of the optics, defined as the half-angle of the FoV circular cone, γ_M .

The large desired aperture calls for an $f/\#$ as small as possible in order to reduce the size of the FS. However the large desired aperture implies, in any case, a large FS size.

5.2.1 Entrance pupil of the optics

The apparatus sensitivity to low signals is affected by a basic and unique sizeable parameter: the optics aperture, that is the entrance pupil area, A_{EP} . Increasing the aperture, to within external constraints, gives a guaranteed improvement of the performance: it is just a matter of technology and money to build such a large apparatus.

As a very large aperture optics is needed a deployable optics is most probably required.

The optics aperture, also fixes the size of the apparatus. The lower limit for A_{EP} is basically set by the requirement on the energy threshold, while the upper limit is fixed by external constraints.

The total number of detected photons is roughly proportional to solid angle subtended by the optics entrance pupil as it is seen by the EAS: $\approx A_{EP}/H^2$. Therefore, for a required energy threshold, the choice of A_{EP} and orbit height is driven by the number of photons that one wants to observe.

5.2.2 FoV of the optics

The large desired aperture implies in any case a large FS size.

In order to gain instantaneous geometrical aperture, either a larger orbit height or a tilt with respect to nadir might be more effective than increasing the FoV. In fact these options might have two beneficial effects: to keep the FS size limited and to ensure a better optics performance, as the performance of the optics tends to become worse, normally, when the FoV increases. In fact the large required FoV and the necessity to keep the optics simple typically give a PSF which is not good enough to detect the lateral EAS dimensions. Even if one manages to get a good enough PSF the required number of channels would increase unacceptably. In our discussion we will consider a FoV aperture (half-angle) $15^\circ \leq \gamma_M \leq 25^\circ$.

5.2.3 Reflective or refractive ?

There are virtues and defects for using refractive versus reflective optics in this kind of experiment. A refractive system is possibly difficult to deploy and a complex supporting structure is required due to the large dimensions. A reflective system would suffer from the obscuration due to the FS and the very limited room for the FS Photo-Detector. The latter might be a real issue, depending on the kind of sensors one is going to use.

On a main drawback of a reflective system is that the curvature of the FS (that is center of curvature of the FS on the opposite side with respect to the incoming light) is such that the filling of the FS with the array of sensors is more difficult and the filling factor tends to be worse than for a refractive system, where the center of curvature of the FS is on the same side with respect to the incoming light.

5.3 Effect of the observation angle (location on the FS)

At the edge of FoV ($\gamma \simeq \gamma_M$) the EAS triggering and reconstruction is much more difficult than near the center of the FoV. In fact due to the larger EAS distance the irradiance (energy/photons per unit area per unit time) decreases as $\approx \cos^2 \gamma$. Moreover the effective entrance pupil typically decreases as $\cos \gamma$: this is the so-called obliquity factor of the optics, due to the fact that the size of the entrance pupil is seen reduced by a factor $\cos \gamma$. As a result the number of photons received on FS by an EAS of fixed energy scales at least as $\cos^3 \gamma$.

In general the real optics triggering efficacy/efficiency, $\varepsilon_O[\gamma]\varepsilon_B[\gamma]$, also decreases while increasing the field-angle. This also includes the effect of the absorption losses inside the refractive materials.

Moreover an EAS detected at the edge of the FoV would suffer from a larger atmospheric attenuation $T_A[\gamma]$ (see equation (7)) due to the longer and more inclined path.

As a smaller number of photons is detected from any EAS when it is observed at the edge of FoV, with respect to the same EAS observed at the center of FoV, one can roughly say that the FoV center (more photons from the EAS, smaller geometrical acceptance) is better for low energy events and low photon flux while the FoV edge (less photons from the EAS, larger geometrical acceptance) is better for high energy events and high photon flux rates.

5.3.1 Signal and RB roll-off with field-angle

It is important to compare the dependence of both signal and RB on the field-angle.

Let us assume an ideal optics, that is an optics such that all the photons hitting the entrance of the optical system are focused inside the desired bucket. For such an optics: $\varepsilon'_O[\gamma] \equiv \varepsilon_O[\gamma]\varepsilon_B[\gamma] = \cos \gamma$. Beware that for a real optics $\varepsilon'_O[\gamma]$ might typically drop faster with γ .

The field-angle dependence for a given source is given by

$$S[\gamma] \sim T_A[\gamma]\varepsilon'_O[\gamma] \cos^2 \gamma \longrightarrow \gamma(0 \rightarrow 25^\circ) : (1.0 \rightarrow 0.72) \quad . \quad (12)$$

On the other hand the field-angle dependence for the RB is given by

$$B[\gamma] \sim \varepsilon'_O[\gamma] \longrightarrow \gamma(0 \rightarrow 25^\circ) : (1.0 \rightarrow 0.87) \quad . \quad (13)$$

Both signal and RB decrease at increasing field-angles, but in a different way. In fact the field-angle dependence for the signal to RB ratio is:

$$\frac{S}{B}[\gamma] \sim T_A[\gamma] \cos^2 \gamma \longrightarrow \gamma(0 \rightarrow 25^\circ) : (1.0 \rightarrow 0.79) \quad . \quad (14)$$

The dependence on the field-angle of both the signal and the signal-to-background ratio renders useless the increase of the optics FoV above a certain extent for a nadir pointing instrument. Similar considerations apply to tilted instruments.

Many parameters (such as the trigger settings) require tuning as a function of the field-angle, that is as a function of the radial distance on the FS.

One important result is this that, as the efficiency curve as a function of the energy roughly scales in energy as the inverse number of signal photons detected, a detection energy threshold at least ≈ 2 times higher is expected for events detected at $\gamma = 25^\circ$ with respect to events detected on-axis [34, 35].

As a conclusion the performances drop significantly at large angles from nadir due to the larger EAS distance, the larger atmospheric absorption and the worse optics photon collection efficiency (the latter actually depends on the angle from the optical axis, not from nadir).

5.3.2 Other considerations

The FoV, together with the satellite altitude, determines the geometrical aperture (discussed in the section 5.7) and therefore the number of events to be detected. The D_{EP} defines the detector collection area and its sensitivity, but also fixes the apparatus size and, consequently, the mass and the volume of the payload.

The diameter D_{PD} of the FS is a function of the FoV (half-angle γ_M) and of the focal length F :

$$D_{PD} = 2F \sin \gamma_M \quad (15)$$

If we introduce the optics f -number, $f/\# \equiv F/D_{EP}$ then

$$D_{PD} = 2f/\# D_{EP} \sin \gamma_M \quad (16)$$

Note that for $\gamma_M = 25^\circ$ and $f/\# = 1$ the FS is as large as the entrance pupil. A further discussion of these arguments can be found in [37].

As the apparatus is basically photon-limited, the entrance pupil shall be as large as possible, up to the limit allowed by external, technological and practical constraints. Therefore the size of the optics will be approximately set to the maximum allowable size. Therefore a reasonable assumption for any real apparatus is that the FS is not larger than the optics: if the latter is approximated by the optics entrance pupil, as it would be desirable for a high-efficiency optics, this implies the rough estimate: $2f/\# \sin \gamma_M \lesssim 1$

5.4 The photo-detector on the FS

As a consequence of the limits on f -number and on the pixel size, a very large area FS is required: the choice of the sensor has to account for this. This basically means that compact and light sensors are required.

The pixel size is driven by two competing requirements: going far away from the Earth (or tilting) requires a smaller pixel size and increasing the optics aperture (and therefore the focal length) implies a larger pixel size.

The overall photo-detection efficiency of the photo-detector is one of the most important parameters affecting the performance. However, needless to say, it cannot increase larger than one. Typical, realistic overall photo-detection efficiencies in the range $(0.1 \div 0.2)$ can be quoted for these kind of apparatus. Even in the most optimistic approach it is not realistic to expect more than a factor ≈ 3 improvement, in the near future, provided huge efforts can be devoted to the development of suitable sensors with higher Quantum Efficiency. In fact the main source of inefficiency, as of today, is typically the rather low Quantum Efficiency, affecting the Total Photo-Detection efficiency of the sensors. However also the geometrical acceptance and filling factor of the array are a crucial issue for this kind of application.

A lot of other factors affects the overall efficiency. They are however all factors already very close to one (typically ≈ 0.9), but the product of many of them can make the overall efficiency drop. In order to make a significant change all of them should be substantially improved because they are already very close to one: there is little hope to gain anything substantial.

5.4.1 The parameters of the Photo-Detector

Approximate relations, useful to estimate the relevant photo-detector parameters, are summarised in this section. The relations in this section will be essentially geometrical, more refined estimates would require a precise design and full simulations.

The characteristics of the optics have a strong impact on the photo-detector design. The Point Spread Function (PSF) of the optics has to match, approximately, the photo-detector pixel size. In fact a finer granularity would allow a better reconstruction, provided enough photons are collected, possibly allowing to measure the PSF itself. However a tradeoff with cost and complexity (driven by the number of channels) is unavoidable. On the other hand, obviously, a pixel size much larger than the PSF would not exploit all the optics performance, wasting the efforts for the optics.

The FS shape and dimensions are determined by the optics. At this stage, therefore, only rough estimates of the corresponding photo-detector parameters will be attempted.

A more careful evaluation can only be carried on once the design of the optics can be better defined.

The desired number of pixels of the photo-detector can be estimated, from the desired parameters, by the relation

$$N \approx \frac{\pi H^2 \tan^2 \gamma}{\Delta L^2} . \quad (17)$$

The required photo-detector pixel size, δ , corresponding to observing a length ΔL on the Earth surface, can be estimated by the relation

$$\delta \approx \frac{f \Delta L}{H} , \quad (18)$$

where f is the focal length of the optics.

The photo-detector surface has to approximate the focal surface of the optics. The latter can be assumed, to a first approximation, to have a spherical shape with radius equal to the focal length of the optics, f , and maximum angular aperture β . Its area is then given by the relation

$$A_{\text{det}} = 2\pi f^2 [1 - \cos \beta] . \quad (19)$$

The FS maximum diameter is given by

$$D_f = 2f \sin \beta . \quad (20)$$

Note that, at least to a first approximation, $\beta \simeq \gamma_M$.

The approximate maximum number of pixels which can be fitted on the FS of the photo-detector is given by the relation

$$n \approx \frac{A_{\text{det}}}{\delta^2} . \quad (21)$$

Alternatively the desired pixel dimension on the FS can be estimated, in terms of the FS parameters and the desired number of pixels one wants to see at the Earth, by the relation

$$d \approx \sqrt{\frac{A_{\text{det}}}{N}} . \quad (22)$$

Note that, to the present level of approximation and with the present parameters, the two relations 18 and 22 are roughly equivalent, given the relations 17 and 19.

The optics also determines the distribution of incidence angles of the photons on the FS, which has some impact on the photo-detector design. The marginal ray angle is determined by the $f\#$ of the optics and is given by the relation

$$\tan \theta_{\text{max}} \approx \frac{1}{2f\#} . \quad (23)$$

The angular granularity of the photo-detector, $\Delta\alpha$, is given by the relations

$$\Delta\alpha \approx \frac{\Delta L}{H} \simeq \frac{\delta}{f} . \quad (24)$$

The solid angle coverage of every pixel, $\Delta\Omega$, is given by

$$\Delta\Omega \approx \frac{\Delta L^2}{H^2} \simeq \frac{\delta^2}{f^2} \simeq [\Delta\alpha]^2 . \quad (25)$$

The approximate defocusing in the direction parallel to the FS, Δw , produced by a small displacement Δz in the direction perpendicular to the FS, is given by the relation

$$\Delta w \approx \Delta z \tan \theta_{\text{max}} = \frac{\Delta z}{2f\#} \ll \delta . \quad (26)$$

In order to reduce the effect of defocusing on the large FS a good fit between the ideal optics FS and the real FS must be implemented. In general it is not trivial to accomplish this because the optics FS has a complex geometrical shape.

5.5 Number of detected photons, efficacy and energy resolution

The required energy resolution ($\Delta E/E \sim (20\% \div 30\%)$) calls for a relative error due to the Poisson statistics of the detected photons not larger than $\sigma_N/N \sim (0.10 \div 0.15)$, assuming an equal contribution from statistical and systematic errors, as it is appropriate for a well-designed apparatus. This implies that at least one hundred photons must be detected from any EAS at the lowest energies, with full triggering efficiency. Obviously the number of detected photons impacts significantly on the other observables as well.

Assuming an ideal optics and the reference EAS one can easily derive the requirements on the optical triggering efficacy from the requirement on the energy resolution. As the angular extension of the reference EAS is short on the FS (see section 5.6) the properties of the apparatus can be considered uniform.

The time-integrated irradiance of the signal reaching the instrument, as a function of θ , is shown in the figures 6 and 7. From the time-integrated irradiance we can infer the required overall triggering efficacy and the minimum apparatus diameter (see section 6). This result does not depend on the implementation of the optical system and the photo-sensor but some assumptions are required in order to proceed. The required overall triggering efficacy for observing the same EAS obviously scales as H^2 .

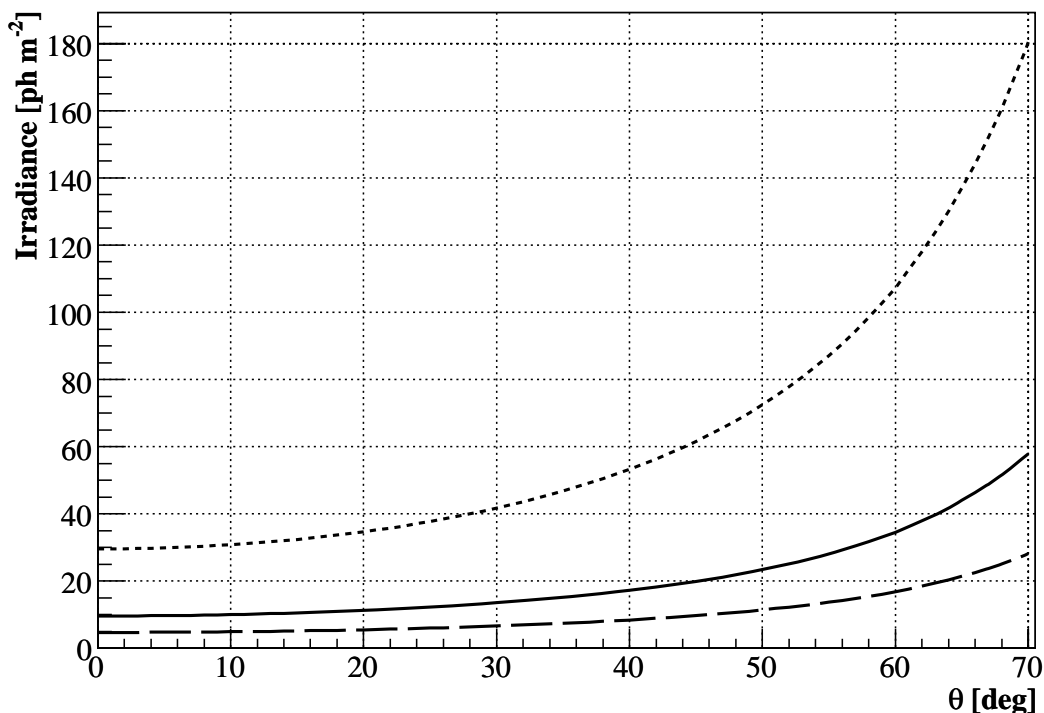


Figure 6: Signal time-integrated irradiance of an EAS as a function of θ ($\psi_{\text{az}} = 90^\circ$ and $\gamma = 15^\circ$). Solid line: $H = 700$ km; dotted line: $H = 400$ km; dashed line: $H = 1000$ km.

5.6 The length and duration of the visible EAS image

The angle subtended by the visible EAS image on the FS of the apparatus as well as its time duration, which are fundamental parameters in the experiment design, are easily estimated by determining the first and last detected points of the EAS.

If one assumes to be able to subtract the background, the shape of the detected photon hits is well described by the Gaisser-Hillas function (5), which is a Gamma distribution in the variable $\hat{X} \equiv X - X_0$:

$$g(\hat{X}) = \frac{1}{\Gamma(\alpha)} \beta^{-\alpha} \hat{X}^{\alpha-1} \exp(-\hat{X}/\beta) \propto \hat{X}^{(X_R/\lambda)} \exp(-\hat{X}/\lambda) \quad (27)$$

$$\text{where } \alpha \equiv \frac{X_R}{\beta} + 1, \quad \beta \equiv \lambda, \quad X_R \equiv X_M - X_0 \quad . \quad (28)$$

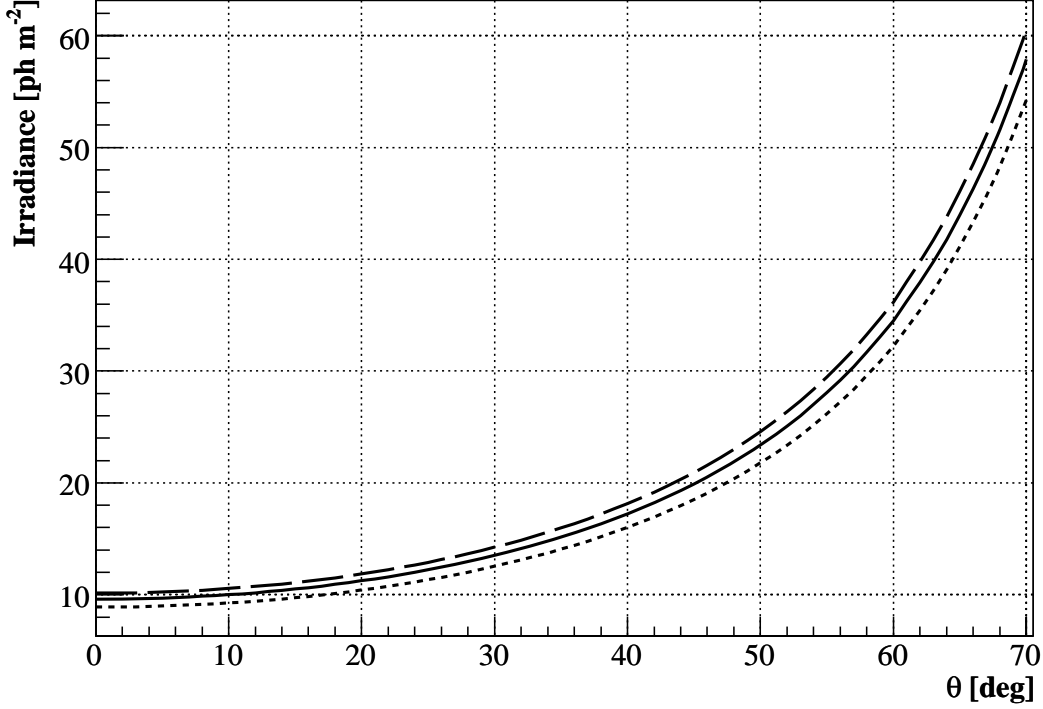


Figure 7: Signal time-integrated irradiance of an EAS as a function of θ ($H = 700$ km and $\psi_{az} = 90^\circ$). Solid line: $\gamma = 15^\circ$; dotted line: $\gamma = 20^\circ$; dashed line: $\gamma = 10^\circ$.

The mean and the standard deviation of this gamma distribution are therefore

$$\begin{aligned}\langle X \rangle &= \alpha\beta = X_M - X_0 + \lambda \\ \sigma_X &= \beta\sqrt{\alpha} = \sqrt{\lambda(X_M - X_0 + \lambda)}\end{aligned}$$

As we require to observe at least $N \simeq 100$ photons in order to get a good enough energy resolution (see section 5.5), the minimum and maximum value and the range of \hat{X} in the distribution are:

$$\begin{aligned}\min(\hat{X}) &\approx \langle \hat{X} \rangle - 2\sigma_{\hat{X}} \\ \max(\hat{X}) &\approx \langle \hat{X} \rangle + 3\sigma_{\hat{X}} \\ \text{range}(\hat{X}) &\approx 5\sigma_{\hat{X}} \quad ,\end{aligned}$$

as it can be quickly determined via simulations of gamma distributions using the physical parameters in section 4.2.

It should be noted that for $N = 100$ the range estimation is $\approx 5\sigma$ for a gaussian distribution also but in that case the distribution is obviously symmetrical with respect to the mean value. However the gamma distribution arising from the current physical parameters has a relatively small skewness⁶ and kurtosis excess⁷ and therefore it is very similar to a gaussian.

Other values are summarized in table 4. The results show that, as expected, the range of the observed photon distribution (that is the observed image length) does not change by a huge amount when changing the photon detection capability. The dependence on the number of observed photons can be fitted by a second degree polynomial.

Simulations with different parameters show that, as expected, the range of the observed photon distribution (that is the observed image length) is not strongly affected by little changes of the physical parameters of the EAS.

⁶The skewness of a gamma distribution is given by $\gamma_1 = 2/\sqrt{\alpha} \approx 0.55$ for a $1 \cdot 10^{19}$ eV proton EAS.

⁷The kurtosis excess of a gamma distribution is given by $\gamma_2 = 6/\alpha \approx 0.46$ for a $1 \cdot 10^{19}$ eV proton EAS.

N	range	$\langle \hat{X} \rangle$ -min	max- $\langle \hat{X} \rangle$
$N = 10$	$(3.05 \pm 0.01)\sigma$	1.4σ	1.7σ
$N = 100$	$(5.01 \pm 0.01)\sigma$	2.0σ	3.0σ
$N = 1000$	$(6.53 \pm 0.01)\sigma$	2.4σ	4.1σ
$N = 10000$	$(7.83 \pm 0.01)\sigma$	2.7σ	5.1σ

Table 4: Range estimation for a gamma function with parameters corresponding to a typical UHECP induced EAS.

One must also take into account that a nearly vertical EAS is truncated by the ground.

It is now easy to estimate the angle ξ_{EAS} subtended by the EAS image on the FS and the EAS image duration T_{EAS} on the FS. The dependence on the EAS zenith angle θ are shown respectively in figures 8÷23.

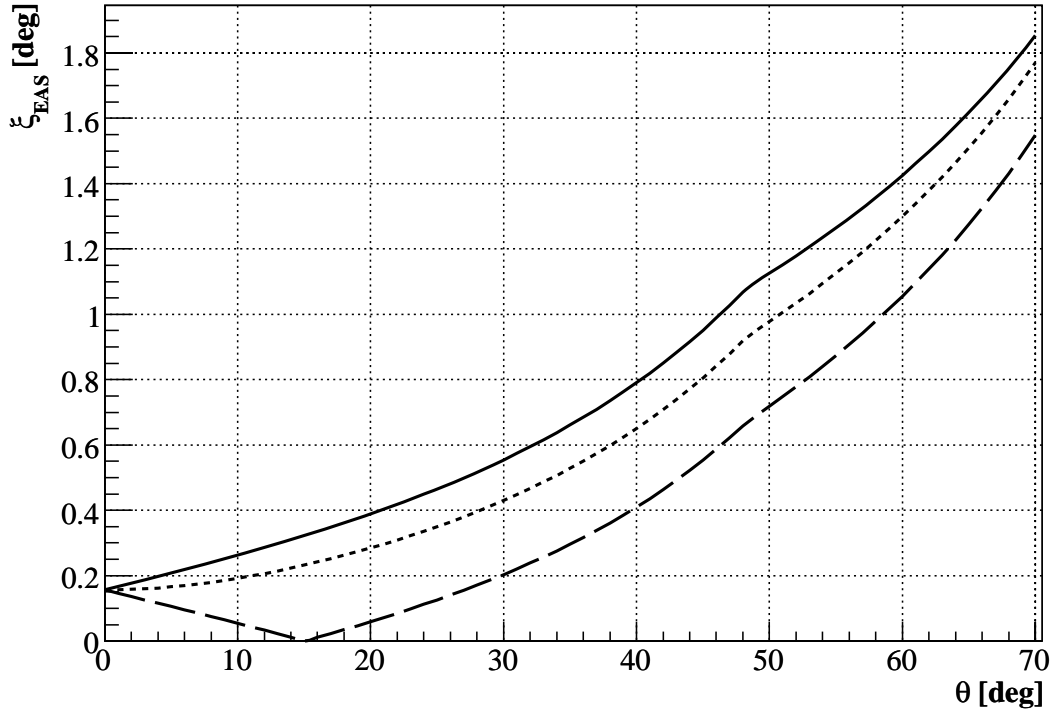


Figure 8: Angular extension of an EAS on the FS as a function of θ ($H = 700$ km and $\gamma = 15^\circ$). Solid line: $\psi_{\text{az}} = 0^\circ$; dotted line: $\psi_{\text{az}} = 90^\circ$; dashed line: $\psi_{\text{az}} = 180^\circ$.

As it is clear from these figures, $\xi_{\text{EAS}} \lesssim 4^\circ$, justifying the assumptions of section 4. Note also that, for $\theta \lesssim 50^\circ$, the EAS are truncated because the EAS hits the ground, as it is evident from the cusps in the figures. Nevertheless the truncation does not affect the reference EAS, for which we requested $N = 100$ photons. Some numerical values for the reference EAS are given in section 6.1.

It is obvious that the time duration of the EAS image is almost independent on both H and γ for a fixed EAS geometry (figures 11, 13, 21 and 23) while the angular length, for the same EAS, will scale as $\sim \cos \gamma / H$ (figures 20 and 22).

5.7 Aperture

5.7.1 Area observed at the Earth

In the case of a nadir pointing apparatus the geometrical area spanned by the FoV at the surface of the Earth is the area of a spherical cap,

$$A_0 = 2\pi R_\oplus^2 (1 - \cos \beta_M) \quad , \quad (29)$$

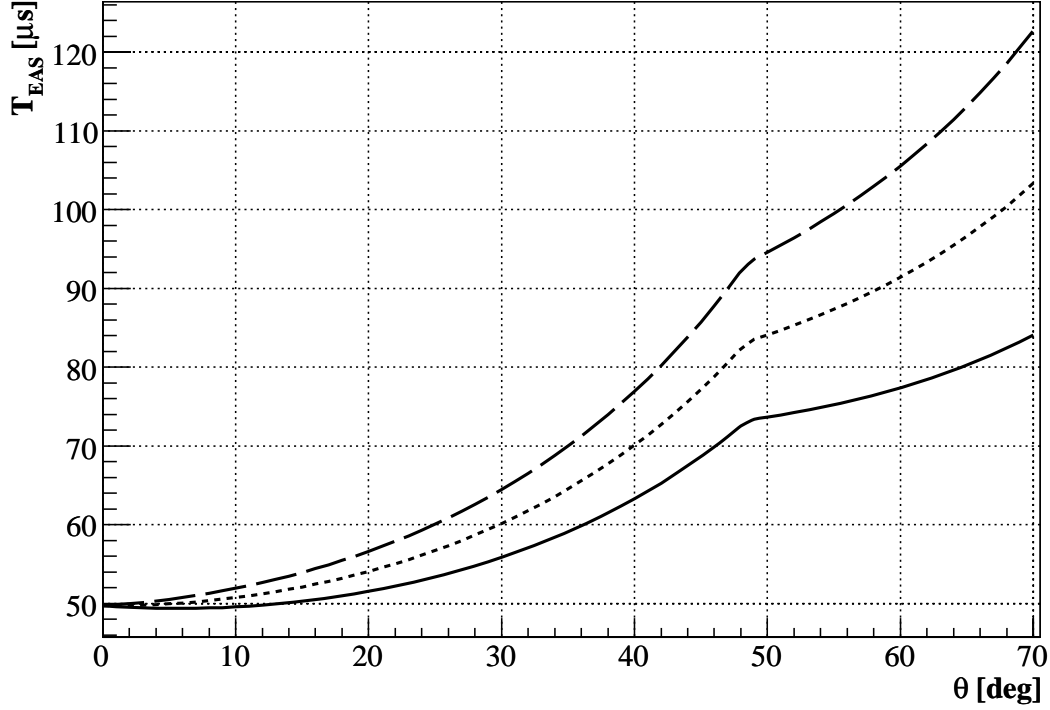


Figure 9: Time duration of an EAS on the FS as a function of θ ($H = 700$ km and $\gamma = 15^\circ$). Solid line: $\psi_{az} = 0^\circ$; dotted line: $\psi_{az} = 90^\circ$; dashed line: $\psi_{az} = 180^\circ$.

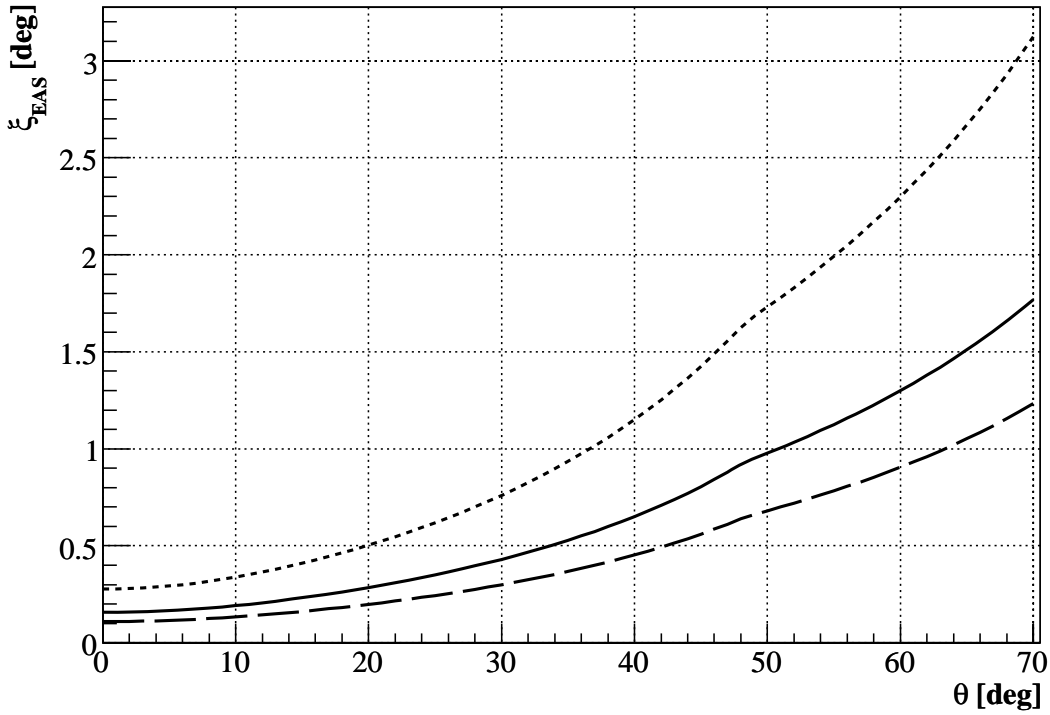


Figure 10: Angular extension of an EAS on the FS as a function of θ ($\psi_{az} = 90^\circ$ and $\gamma = 15^\circ$). Solid line: $H = 700$ km; dotted line: $H = 400$ km; dashed line: $H = 1000$ km.

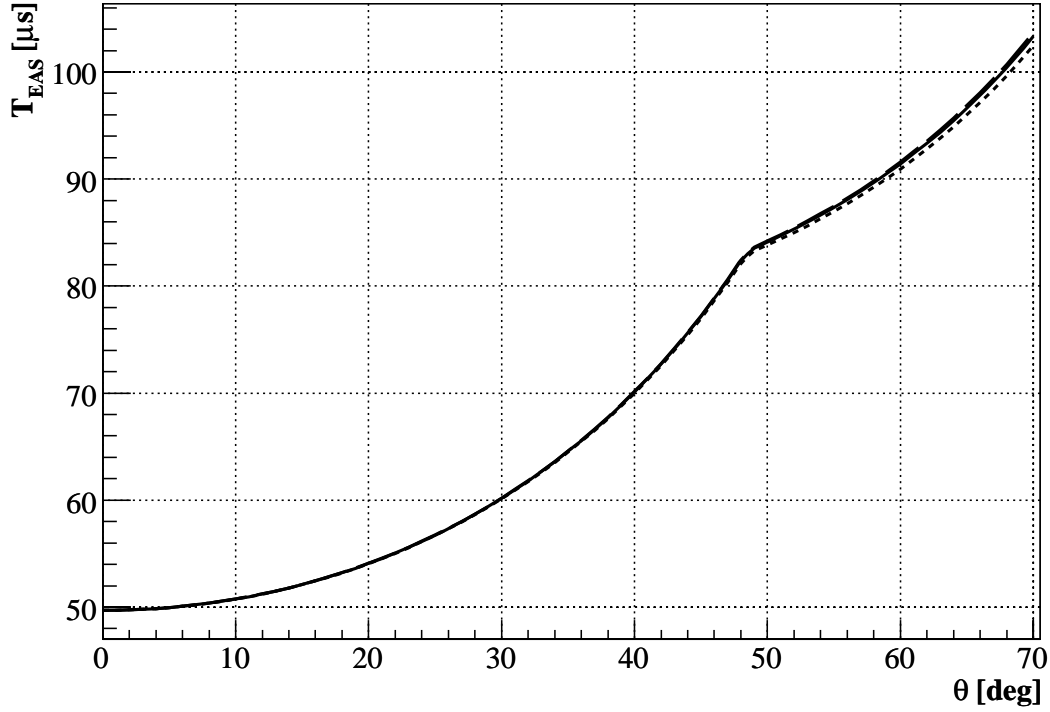


Figure 11: Time duration of an EAS on the FS as a function of θ ($\psi_{az} = 90^\circ$ and $\gamma = 15^\circ$). Solid line: $H = 700$ km; dotted line: $H = 400$ km; dashed line: $H = 1000$ km.

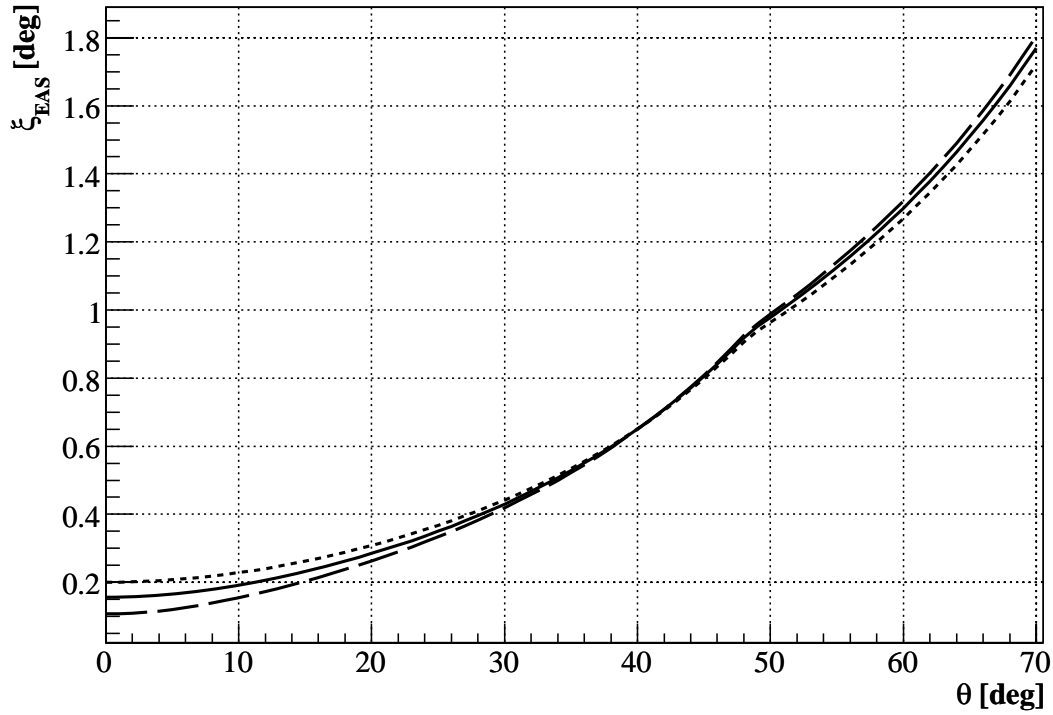


Figure 12: Angular extension of an EAS on the FS as a function of θ ($H = 700$ km and $\psi_{az} = 90^\circ$). Solid line: $\gamma = 15^\circ$; dotted line: $\gamma = 20^\circ$; dashed line: $\gamma = 10^\circ$.

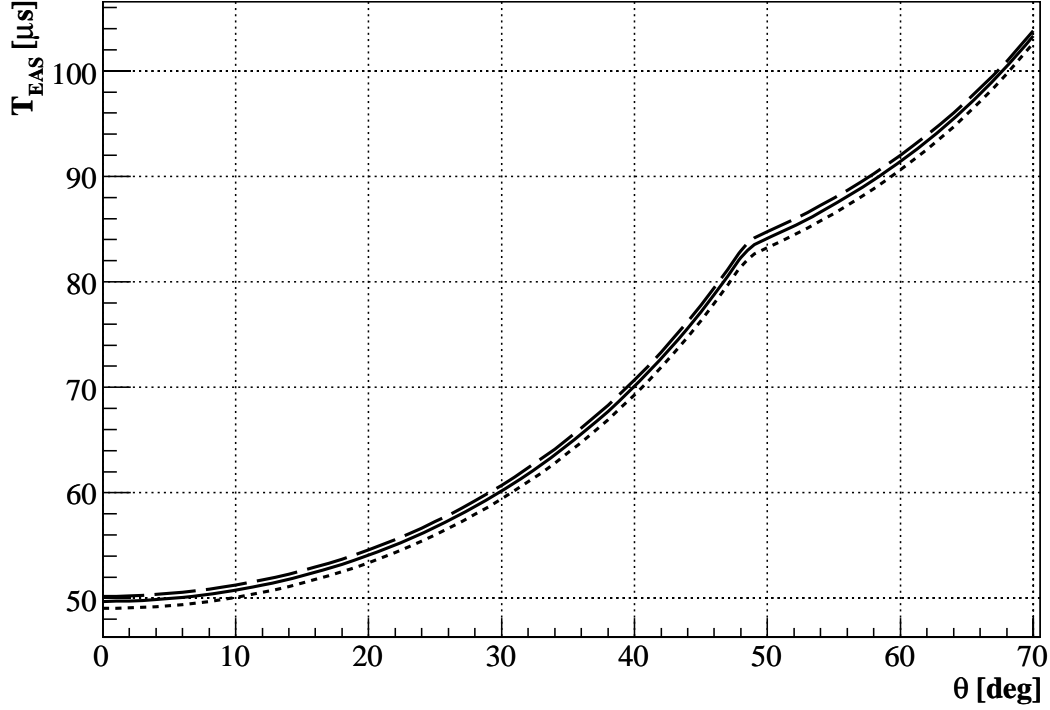


Figure 13: Time duration of an EAS on the FS as a function of θ ($H = 700$ km and $\psi_{az} = 90^\circ$). Solid line: $\gamma = 15^\circ$; dotted line: $\gamma = 20^\circ$; dashed line: $\gamma = 10^\circ$.

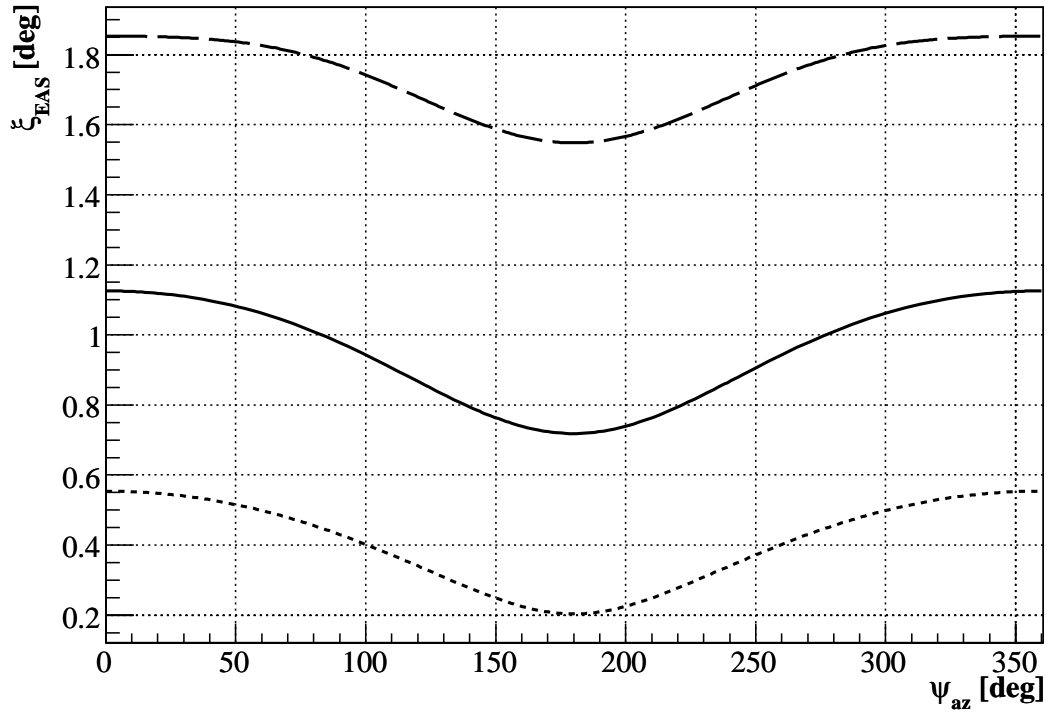


Figure 14: Angular extension of an EAS on the FS as a function of ψ_{az} ($H = 700$ km and $\gamma = 15^\circ$). Solid line: $\theta = 50^\circ$; dotted line: $\theta = 30^\circ$; dashed line: $\theta = 70^\circ$.

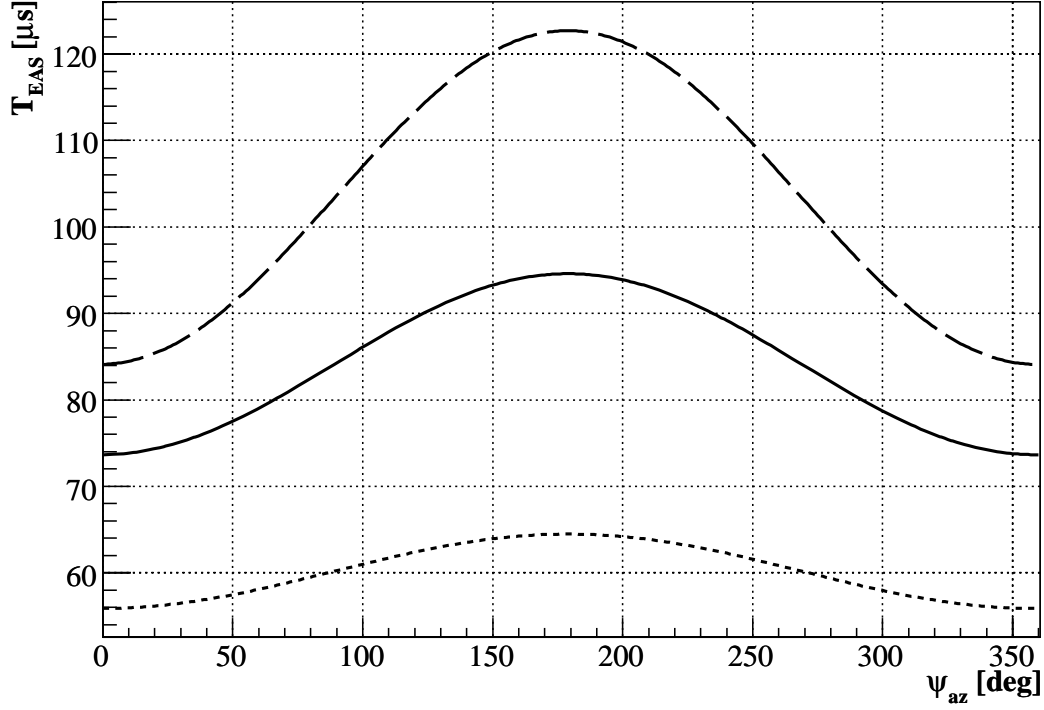


Figure 15: Time duration of an EAS on the FS as a function of ψ_{az} ($H = 700$ km and $\gamma = 15^\circ$). Solid line: $\theta = 50^\circ$; dotted line: $\theta = 30^\circ$; dashed line: $\theta = 70^\circ$.

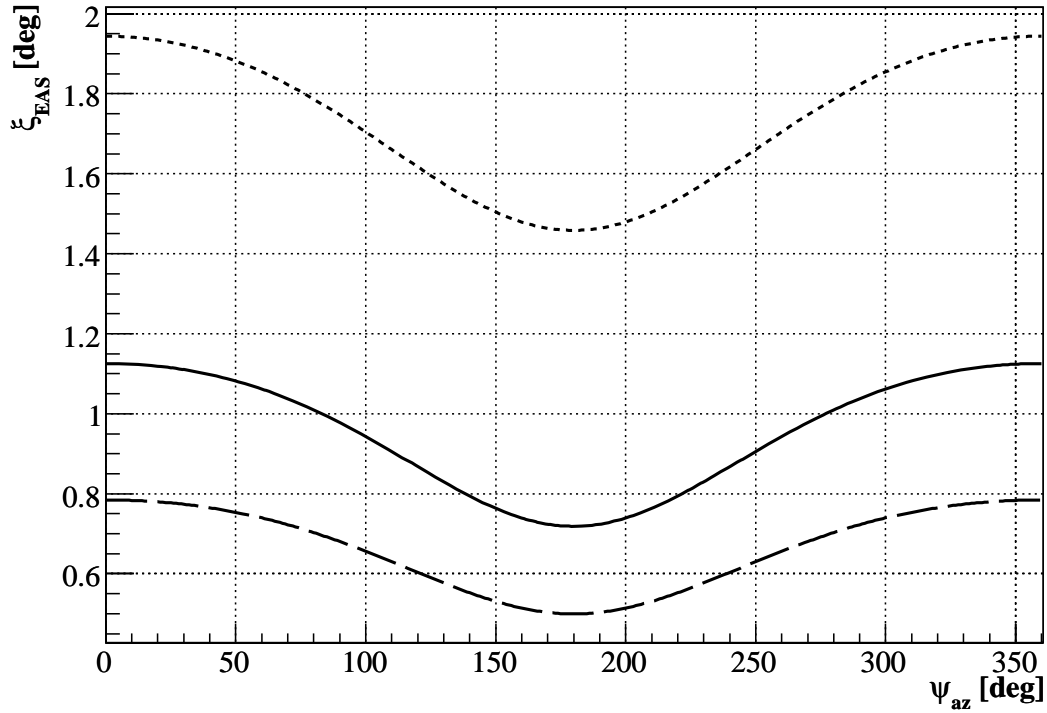


Figure 16: Angular extension of an EAS on the FS as a function of ψ_{az} ($\theta = 50^\circ$ and $\gamma = 15^\circ$). Solid line: $H = 700$ km; dotted line: $H = 400$ km; dashed line: $H = 1000$ km.

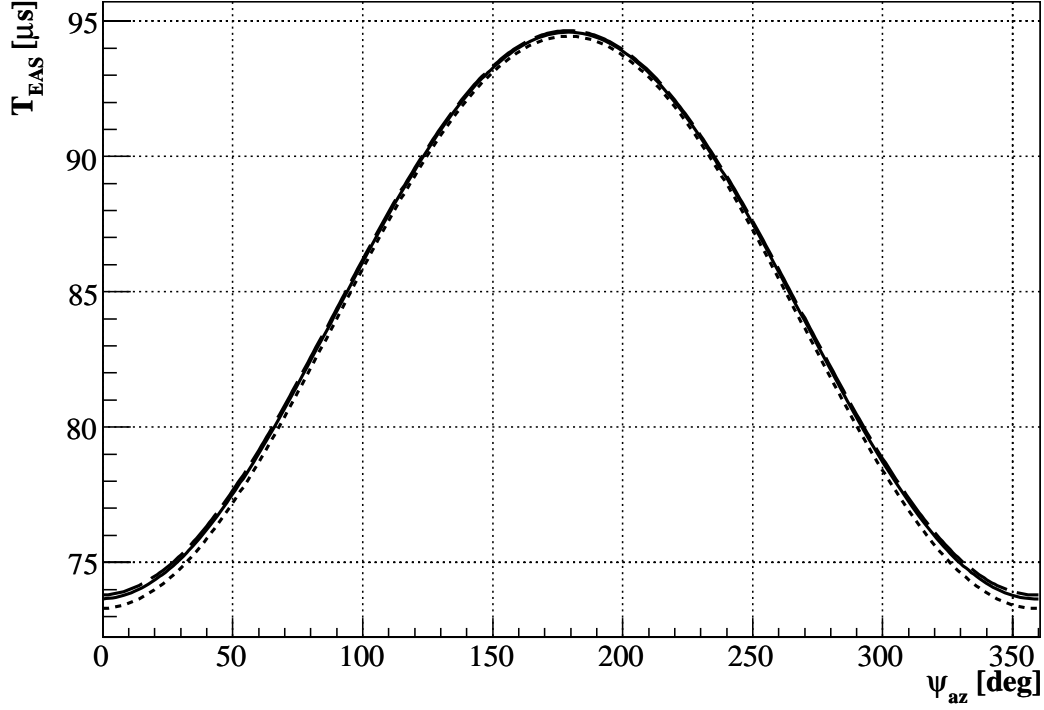


Figure 17: Time duration of an EAS on the FS as a function of ψ_{az} ($\theta = 50^\circ$ and $\gamma = 15^\circ$). Solid line: $H = 700$ km; dotted line: $H = 400$ km; dashed line: $H = 1000$ km.

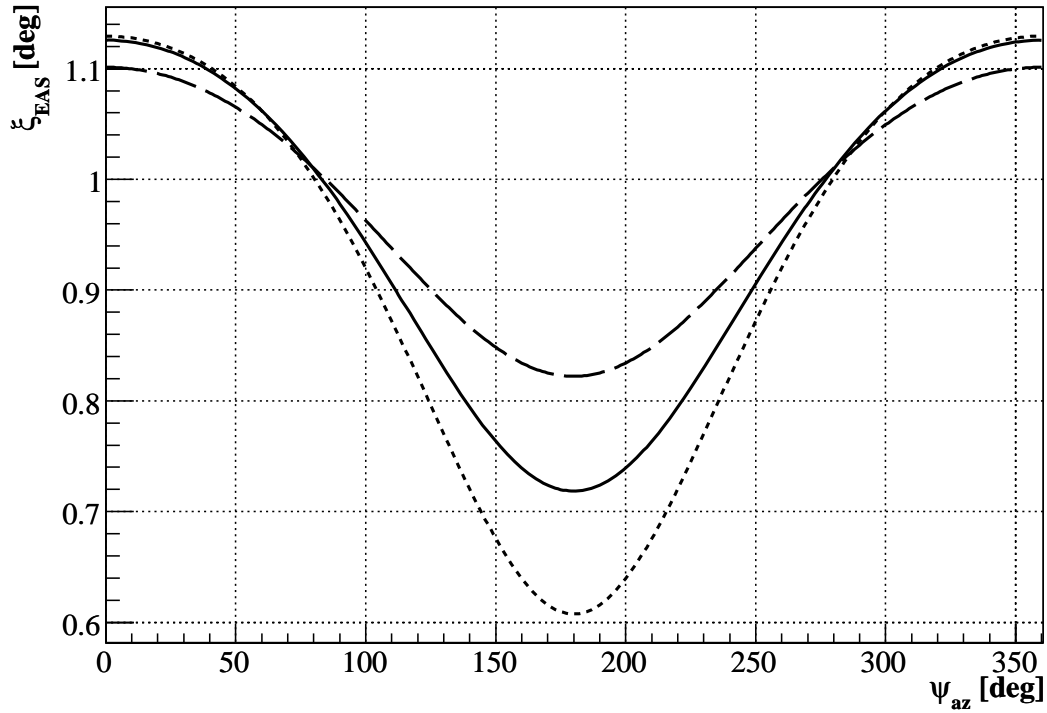


Figure 18: Angular extension of an EAS on the FS as a function of ψ_{az} ($H = 700$ km and $\theta = 50^\circ$). Solid line: $\gamma = 15^\circ$; dotted line: $\gamma = 20^\circ$; dashed line: $\gamma = 10^\circ$.

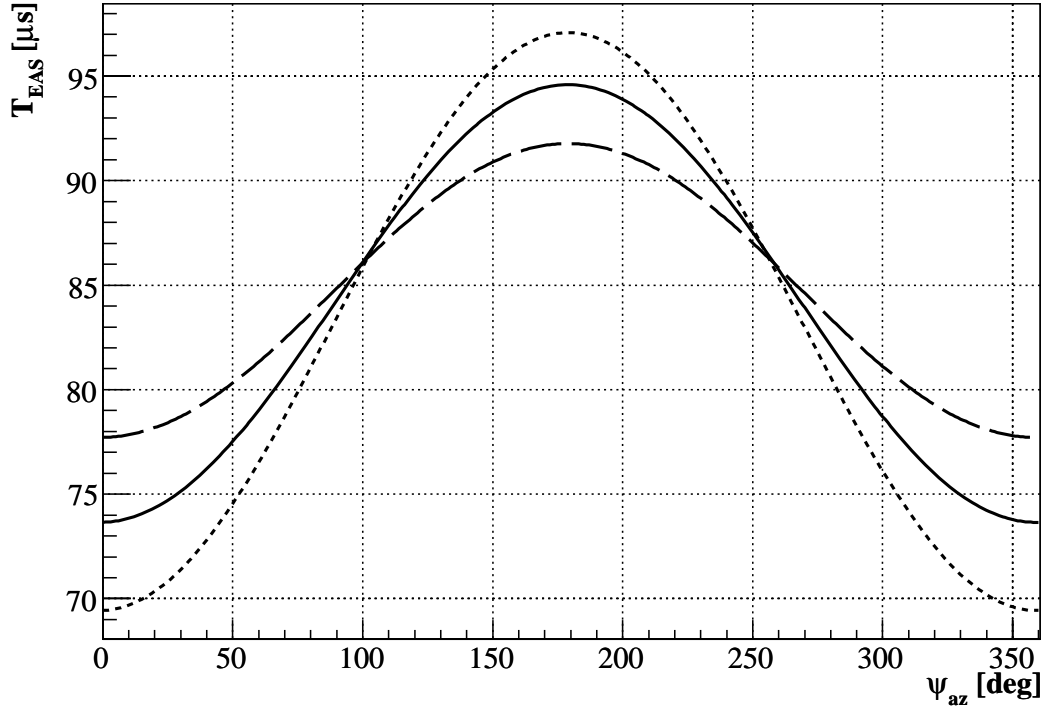


Figure 19: Time duration of an EAS on the FS as a function of ψ_{az} ($H = 700$ km and $\theta = 50^\circ$). Solid line: $\gamma = 15^\circ$; dotted line: $\gamma = 20^\circ$; dashed line: $\gamma = 10^\circ$.

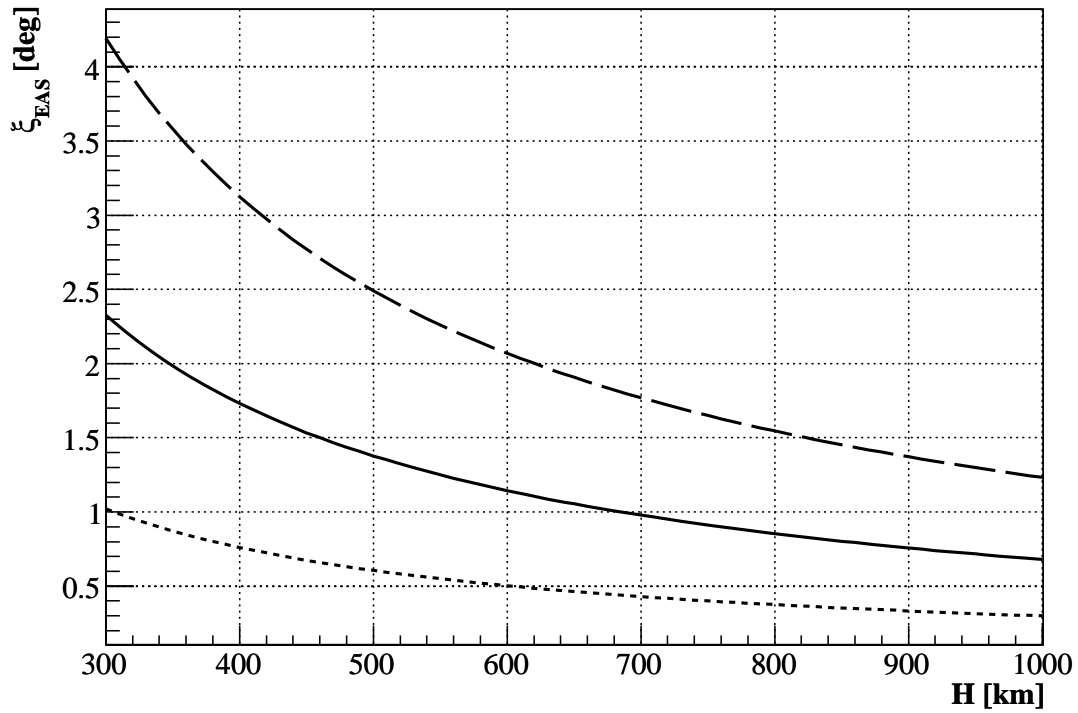


Figure 20: Angular extension of an EAS on the FS as a function of H ($\psi_{az} = 90^\circ$ and $\gamma = 15^\circ$). Solid line: $\theta = 50^\circ$; dotted line: $\theta = 30^\circ$; dashed line: $\theta = 70^\circ$.

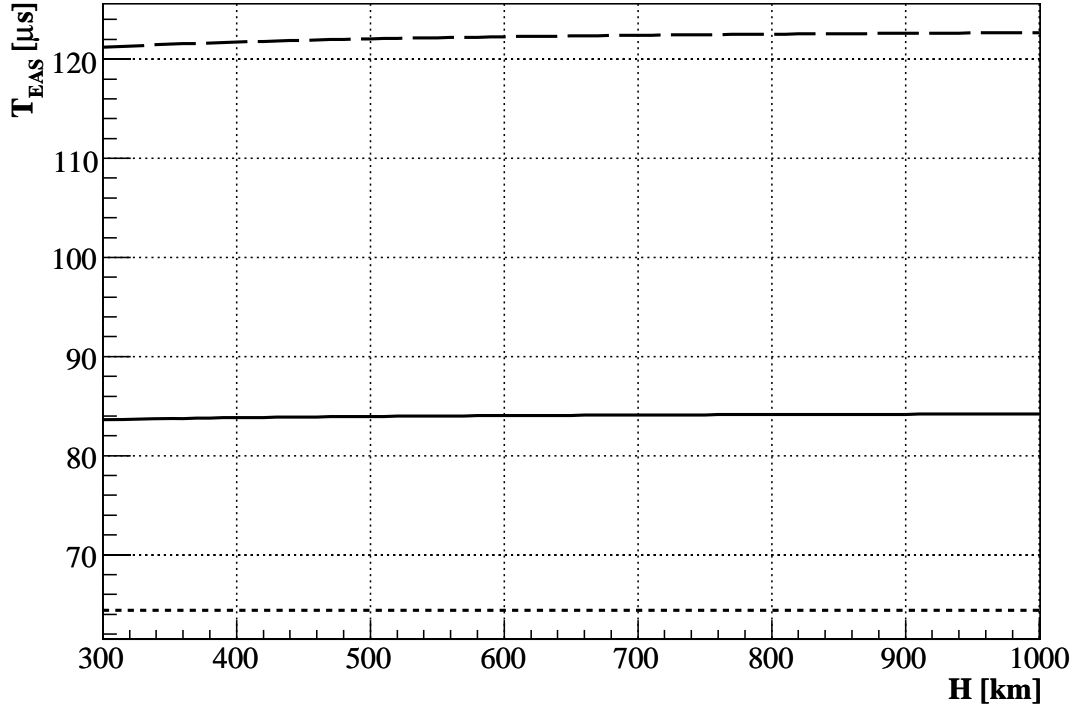


Figure 21: Time duration of an EAS on the FS as a function of H ($\psi_{az} = 90^\circ$ and $\gamma = 15^\circ$). Solid line: $\theta = 50^\circ$; dotted line: $\theta = 30^\circ$; dashed line: $\theta = 70^\circ$.

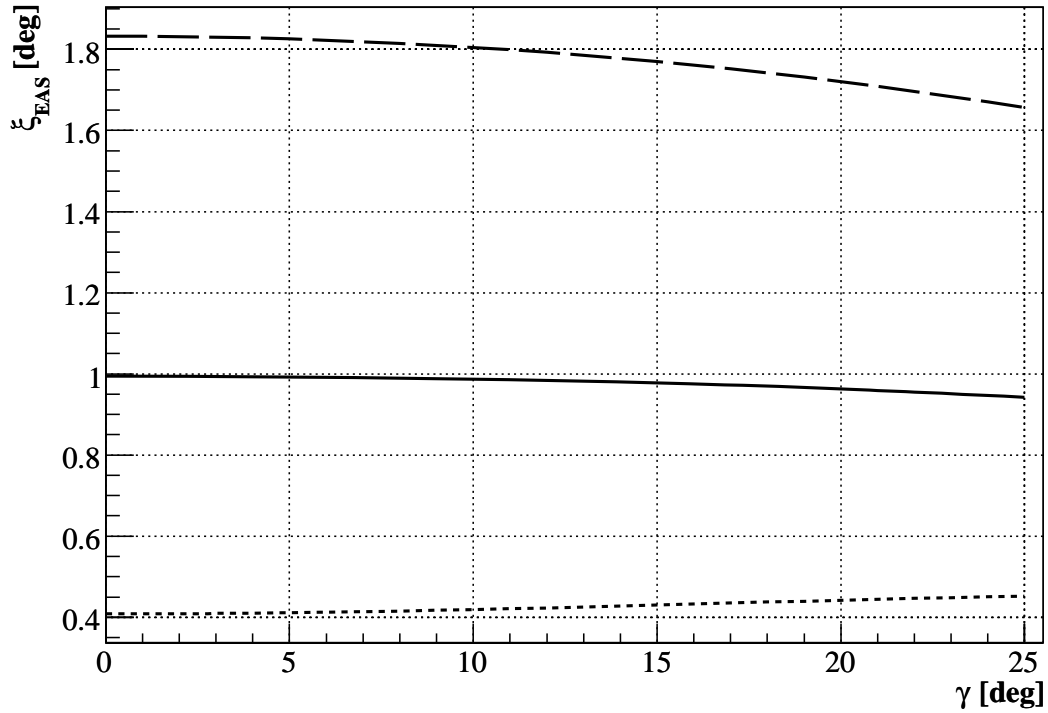


Figure 22: Angular extension of an EAS on the FS as a function of γ ($H = 700$ km and $\psi_{az} = 90^\circ$). Solid line: $\gamma = 15^\circ$; dotted line: $\gamma = 20^\circ$; dashed line: $\gamma = 10^\circ$.

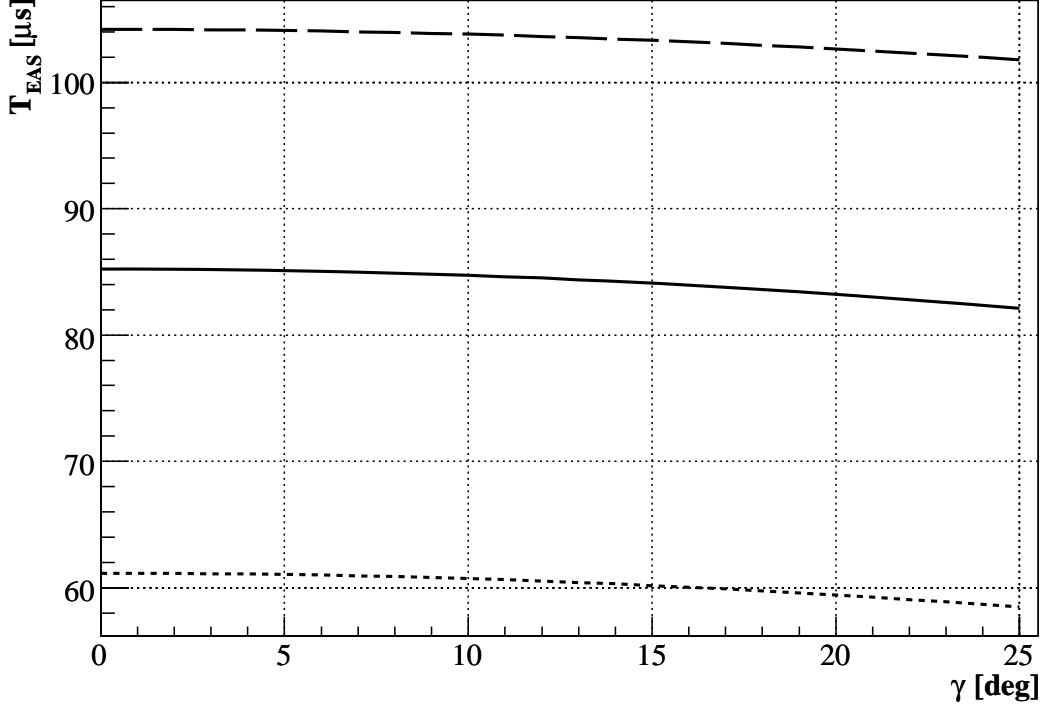


Figure 23: Time duration of an EAS on the FS as a function of γ ($H = 700$ km and $\psi_{az} = 90^\circ$). Solid line: $\gamma = 15^\circ$; dotted line: $\gamma = 20^\circ$; dashed line: $\gamma = 10^\circ$.

in terms of H , the orbital height, R_\oplus , the Earth radius, γ_M the half-angle FoV of the apparatus, and β_M , the angle at Earth center between nadir and the FoV border which is given by:

$$\beta_M = \arcsin\left(\frac{R_\oplus + H}{R_\oplus} \sin \gamma_M\right) - \gamma_M \quad . \quad (30)$$

From A_0 it is easy to estimate the total target mass, M , using the value of the vertical column density of air (~ 1033 g/cm²). In table 5 some numbers are given for different values of H and γ_M . An approximated value for the area, using the flat Earth approximation is

$$A_0 = \pi H^2 \tan^2 \gamma_M \quad . \quad (31)$$

H [km]	γ_M [$^\circ$]	A_0 [$1 \cdot 10^5$ km ²]	M [$1 \cdot 10^{15}$ kg]
400	20	0.67	0.7
700	20	2.07	2.1
1000	20	4.25	4.4
700	15	1.11	1.2
700	25	3.43	3.5

Table 5: Area observed at the Earth and atmosphere mass target.

5.7.2 Instantaneous geometrical aperture

The instantaneous geometrical aperture is defined as:

$$\mathcal{A}_g \equiv \int_A \int_\Omega \hat{v}(\theta, \varphi) \cdot \hat{n} d\Omega dA \quad , \quad (32)$$

in terms of the normalized velocity vector, $\hat{v}(\theta, \varphi)$, of the EAS and the normal unit vector to the surface, \hat{n} .

The effective aperture, for a flat Earth, of a nadir pointing apparatus, only considering EAS which reach ground inside the FoV, is approximately given by the relation:

$$\mathcal{A}_e = \eta_o \eta_c (1 - \tau_{\text{dead}}) \mathcal{A}_g \approx \eta_o \eta_c (1 - \tau_{\text{dead}}) \pi^2 H^2 \tan^2 \gamma_M \quad , \quad (33)$$

in terms of the orbital height, H , the half-angle FoV γ_M , the observational duty cycle η_o , the dead time τ_{dead} and the cloud coverage efficiency ($\eta_c \sim 0.5$), quantifying the effect of real cloud coverage on the EAS detection efficiency. The expression above also gives the effective high energy (asymptotic) aperture, that is the effective aperture when the total detection efficiency equals one.

5.7.3 Tilting of the apparatus

The instantaneous geometrical aperture can increase if the apparatus is tilted with respect to the local nadir by some angle α_{tilt} . In order to evaluate it one needs to estimate the area observed at ground with a tilted apparatus. As the geometrical solution of the problem to find the intersection area of the circular FoV cone with the spherical Earth surface is not trivial at all, the easiest way is to use a simple Monte-Carlo integration.

The Monte-Carlo results for the intersection area, as a function of α_{tilt} , are shown in the figures 24 and 25. It should be noted that the corresponding horizon angle is

$$\beta_{\text{hor}} = \arcsin \frac{R_{\oplus}}{R_{\oplus} + H} \approx \begin{cases} 70^\circ & \text{at } H = 400 \text{ km,} \\ 64^\circ & \text{at } H = 700 \text{ km,} \\ 60^\circ & \text{at } H = 1000 \text{ km} \end{cases} \quad ,$$

which must be taken into account when considering the possible titling angles.

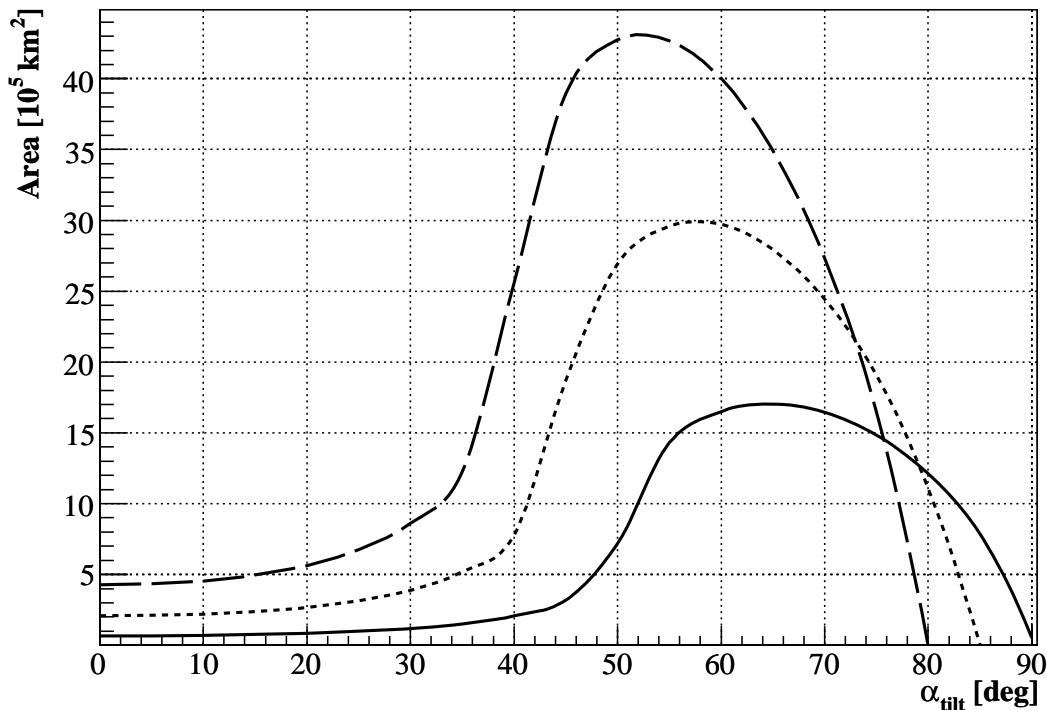


Figure 24: Area seen by the detector at the Earth surface versus α_{tilt} for $\gamma_M = 20^\circ$. Solid line: $H = 400 \text{ km}$ ($\beta_{\text{hor}} \approx 70^\circ$), dotted line $H = 700 \text{ km}$ ($\beta_{\text{hor}} \approx 64^\circ$), dashed line: $H = 1000 \text{ km}$ ($\beta_{\text{hor}} \approx 60^\circ$).

Tilted mode allows to tune the instantaneous geometrical aperture, up to a factor (3 ÷ 5). While titling the apparatus is an effective way to increase the instantaneous geometrical aperture this is not the only important issue which comes into play. In fact the main drawbacks of tilting are that one is observing EAS at a larger and larger distance when looking at the far extreme of the FoV, with a drastically increasing atmospheric absorption. This means that the effective energy threshold in the far part of the FoV increases. Moreover the FoV is highly

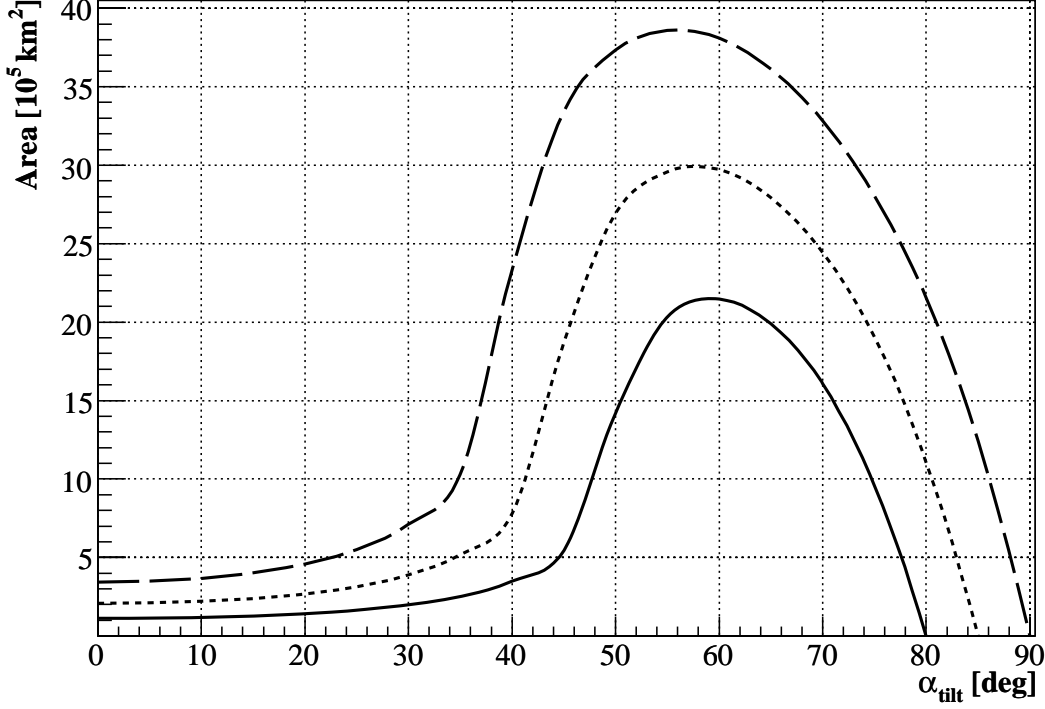


Figure 25: Area seen by the detector at the Earth surface versus α_{tilt} for $H = 700$ km. Solid line: $\gamma_M = 15^\circ$, dotted line $\gamma_M = 20^\circ$, dashed line: $\gamma_M = 25^\circ$.

non uniform and the angular resolution at the far extreme becomes worse unless the pixel size is reduced. The large FoV of the optics, together with the large atmospheric target observed, would require an excellent stray-light control for a tilted apparatus due to the large amount of light entering the FoV. Tilting, together with the large FoV, would also strongly affect the duty cycle, as the large area observed at the Earth would more often include day-time areas.

On the other hand increasing the orbit height seems to be a more effective method to increase the instantaneous geometrical aperture while minimizing the drawbacks mentioned above. In fact one would have no losses from the increased atmospheric transmission and a more uniform FoV and would benefit from smaller required FoV in the optical design.

5.7.4 Duty cycle

It is not easy to estimate the duty-cycle of a space-based apparatus. A dedicated measurement is possibly required.

The major limitation to the apparatus observational duty cycle⁸ comes from the Sun light and the Moon light. The fraction of time in which the detector is unable to operate due to the Sun or the Moon depends on the orbital elements and, during the moontime, on the maximum background rate the detector for which data taking is still possible. For an orbital height $H \sim 400$ km, an orbital inclination of $\sim 50^\circ$ and requiring both the Sun and the Moon to be safely below the horizon, the average duty cycle is $\eta_o \sim 13\%$. If we accept an additional background flux of $100 \text{ ph m}^{-2} \text{ ns}^{-1} \text{ sr}^{-1}$ due to the moonlight, we have $\eta_o \sim 19\%$ [38].

The duty cycle may be influenced by other man-made or natural sources. They will be discussed in section 5.10

Observation duty cycle is driven by the acceptable background level. Therefore it is, in principle, energy dependent but a very good knowledge of the apparatus is required.

5.8 Pixel size and angular resolution

Any EAS will be seen as a point moving inside the FoV with a kinematics (direction and an angular velocity) determined by the EAS direction relative to the line of sight from the instrument to the EAS instantaneous

⁸The observational duty cycle is defined as the fraction of time with the apparatus on, open and taking data.

position. The direction of the EAS velocity vector, as seen by the detector, can be decomposed into two components: one parallel to the line of sight and the other lying in the plane perpendicular to it. The EAS develops approximately at the speed of light and its distance can be considered as a known value, in the case of a space-experiment. Therefore both of them can be reconstructed from the two-dimensional image on the FS plus the timing information. The latter is inferred from the direction and angular velocity of the EAS inside the FoV.

The pixel size, δ , is driven by the Scientific Requirements and constrained by available resources. In particular it affects:

- the EAS reconstruction efficiency and the signal contamination: the number of signal photons divided by the number of RB photons on the pixel roughly scales as $S/B \sim 1/\delta$ for a pixel much larger than the EAS track width on the FS (which basically depends on the optics PSF) while it saturates to a constant for a small enough pixel size;
- the angular resolution;
- the X_M resolution.

It should be kept in mind that due to the relatively small EAS transverse dimensions the EAS image transverse dimensions on the FS will be determined by the PSF only.

A pixel size much larger than the optics PSF would spoil the angular resolution. On the other hand a pixel size smaller than the optics PSF might be useful, in case one has many photons per pixel to improve, via a suitable fitting procedure, the angular resolution.

A pixel size roughly of the same size of the optics PSF turns out to be, usually, a good compromise.

The number of pixels has a strong impact on the Instrument budgets and complexity. A trade-off on the pixel size is therefore very important.

An approximate and simplified analysis, leading to determine the required pixel size, is presented below. Note that the following elementary analysis ignores the effect of the background (making the angular resolution worse) and assumes to have an unbiased estimator of the EAS arrival direction. Therefore the requirements which are derived must be considered as necessary requirements. On the other hand the use of the diffusely reflected Cherenkov flash might improve the angular resolution.

5.8.1 Angular resolution perpendicular to the line of sight

The expected angular resolution $\Delta\beta_{\perp}$ on the EAS direction perpendicularly to the line of sight is readily estimated by assuming to perform a linear fit. The error on the angle can be calculated from the standard relations for a linear least squares fit as:

$$\Delta\beta_{\perp} = \frac{\delta}{\sqrt{12}} \frac{1}{\sigma_{\xi}} \frac{1}{\sqrt{N}} \quad , \quad (34)$$

where N is the number of detected photons, σ_{ξ} is the standard deviation of the observed longitudinal photon distribution along the EAS image (easily determined from the methods presented in section 5.6) and δ is the uncertainty in the position on the FS which can be roughly taken as the pixel size.

Using again the sample EAS (table 2) and exploiting the Gamma-like shape (Gaisser-Hillas function) of the EAS longitudinal profile, the relation between the observed (angular) EAS length, ξ_{EAS} , (i.e. the range of the sampled values) and σ_{ξ} turns out to be $\xi_{\text{EAS}} \approx 5\sigma_{\xi}$ (for $N = 100$), as discussed in section 5.6. Therefore one finds that, in order to reach an angular resolution of the order of $\Delta\beta_{\perp} \sim 1^{\circ}$, a FoV granularity of $\delta \sim 0.1^{\circ}$ is required.

Note that the above result is consistent with the naive estimate:

$$\Delta\beta_{\perp} \approx \frac{\delta}{\xi_{\text{EAS}}} \frac{1}{\sqrt{N}} \quad . \quad (35)$$

The angular resolution $\Delta\beta_{\perp}$ as a function of θ , is shown in figure 26.

5.8.2 Angular resolution parallel to the line of sight

The relation between the observed angular velocity $\omega_{\mathcal{EAS}}$ and the angle β between the EAS velocity vector and the line of sight is the well known relation [30, 29]:

$$\omega_{\text{EAS}} = \frac{c}{D} \left(\frac{1 - \cos\beta}{\sin\beta} \right) = \frac{c}{D} \tan\left(\frac{\beta}{2}\right) \quad (36)$$

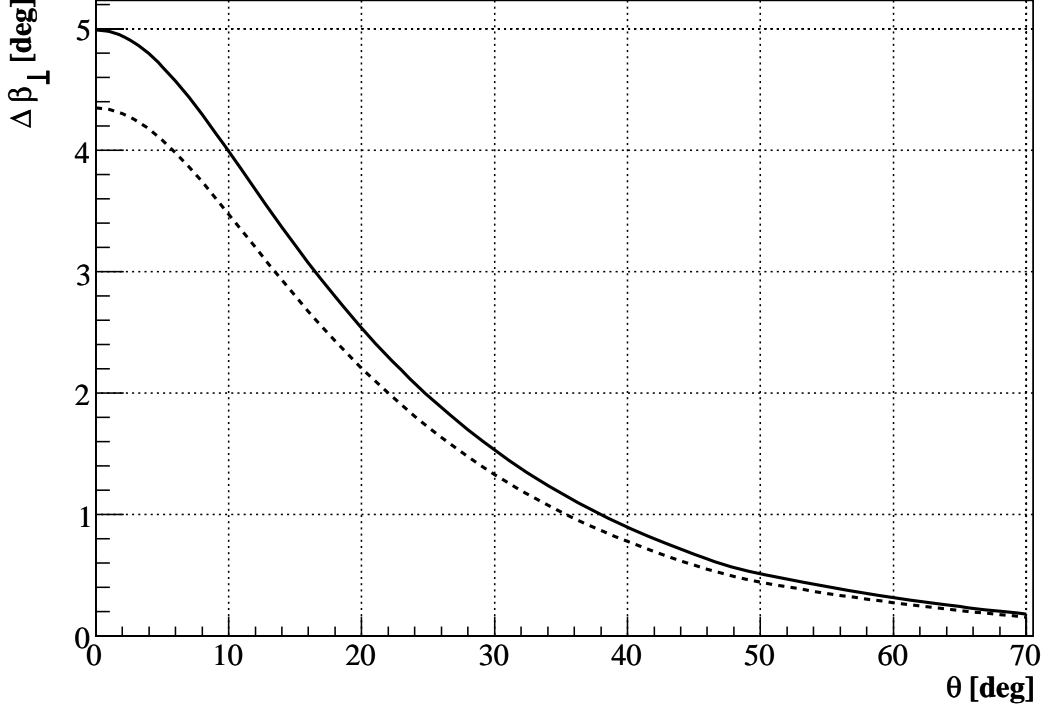


Figure 26: Angular resolution $\Delta\beta_{\perp}$ as a function of θ in the reference conditions. Solid line: $H = 700$ km; dotted line: $H = 400$ km (the line for $H = 1000$ km is very close to the first one).

where c is the speed of light and D is the distance of the EAS.

In the present case, one assumes that the EAS develops in the lower layers of the atmosphere, within ~ 15 km from the ground, so that D is approximately known (the relative error is $\Delta D/D \lesssim 0.05$). Due the non-linear relations between $\omega_{\mathcal{EAS}}$ and β the estimation of the best fit error is more complex in this case. Therefore the error on β is estimated by assuming a simple measurement of the angular velocity of the EAS. One obtains:

$$\Delta\beta_{\parallel} = \frac{\Delta\omega_{\mathcal{EAS}}}{\omega_{\mathcal{EAS}}} = \left(\frac{\delta}{\xi_{\mathcal{EAS}}} + \frac{\delta_T}{T_{\mathcal{EAS}}} \right). \quad (37)$$

For the typical EAS of table 2, by assuming an EAS sampling time not larger than $\delta_T \sim 2.5 \mu\text{s}$, the second term is smaller than the first one. One finds $\Delta\beta_{\parallel} \approx 0.15 \text{ rad} \approx 10^\circ$ by assuming again $\delta \sim 0.1^\circ$. One might assume that, with a best fit, this results will scale as $N^{-1/2}$ obtaining the desired $\Delta\beta_{\parallel} \approx 0.015 \text{ rad} \approx 1^\circ$. Therefore one finds that, in order to aim to get an angular resolution of the order of $\Delta\beta_{\parallel} \sim 1^\circ$, one needs $\delta \sim 0.1^\circ$ and $\delta_T \sim 2.5 \mu\text{s}$.

Note that, as long as δ_T is smaller than the pixel transit time the error is dominated by the pixel size and not by timing. Moreover one might assume that, with a best fit, this results will scale as $N^{-1/2}$.

The angular resolution $\Delta\beta_{\parallel}$ as a function of θ , is shown in figure 27. Some numerical estimates are given in the section 6.3.

5.9 X_M resolution

The requirement on ΔX_M is satisfied following the previous requirements. In fact the relation between slant depth X and the coordinate along the EAS, ℓ , is, in the approximation (2) and neglecting the Earth curvature, is:

$$\left| \frac{dX}{d\ell} \right| = \frac{|\cos \theta|}{h_0} X. \quad (38)$$

Therefore for S_{ref} the $\Delta\ell$ corresponds $\Delta X_M \sim 35 \text{ g/cm}^2$ ($X_M \sim 824 \text{ g/cm}^2$) is larger than 0.5 km. Therefore, neglecting the geometrical and kinematical details of the EAS development, it is larger than half the pixel size

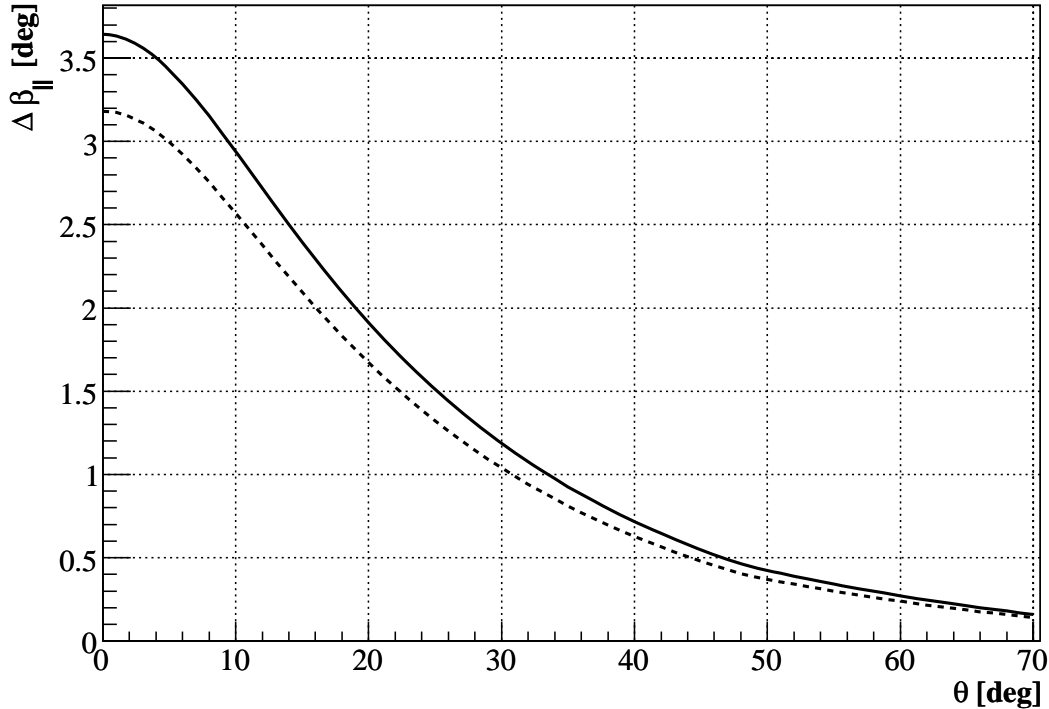


Figure 27: Angular resolution $\Delta\beta_{\parallel}$ as a function of θ in the reference conditions. Solid line: $H = 700$ km; dotted line: $H = 400$ km (the line for $H = 1000$ km is very close to the first one). We assumed $\delta_T \sim 1 \mu\text{s}$.

projected at the Earth⁹. The required X_M resolution is therefore compatible with the pixel size. An improved resolution of $X_M \sim 20 \text{ g/cm}^2$ might be reached by a suitable fitting procedure.

5.10 Noise and background

The RB in the wavelength range WR is estimated from the results of the experiments BABY [39], NIGHTGLOW [40], Arizona-Airglow [41] and the Universitetsky-Tatiana microsatellite [42].

The noise level generated by all the parts of the experimental apparatus has to be kept well below the physical background level, due to the faintness of the air scintillation signal.

The total RB rate intercepted by the apparatus (on the whole entrance pupil and full FoV) is:

$$\nu_{\text{tot}}^{\text{b}} = BA\pi \sin^2 [\gamma_M] \quad . \quad (39)$$

A typical value for the total rate of RB hits detected by the apparatus is of the order of a few hundreds of MHz (see section 6.4). Therefore the intrinsic noise of the whole apparatus (all sources) is required to be less than a few GHz (over the whole Photo-Detector) in order to be negligible with respect to the RB. Note that this requirement should also include the stray-light coming from lack of light-tightness of the apparatus.

In order to detect the faintest EAS reaching the required energy threshold it is mandatory to subtract online the RB as its rate is significant with respect to the air scintillation signal. Therefore a continuous monitoring of the average background on a pixel-by-pixel basis is, most likely, unavoidable to go low in energy in order to have a measure of the RB on the space-time scale comparable to the space-time scale of the EAS development.

As a preliminary step for a space-based mission it is therefore necessary to carry on a detailed characterization of the RB, on the space-time scale of the EAS development, to improve our knowledge of it and improve background rejection [43].

Many experiments have measured this quantity. However in order to devise a method for online background subtraction it is mandatory to have a finer characterization of the space-time behavior of the RB on the space-time scale of the EAS development: $\Delta\alpha \simeq 0.1^\circ$ and $\Delta t \simeq \mu\text{s}$. It is important to stress that the characterization should include measurements along different directions from nadir to cope with off-field RB.

⁹For an orbital height $H \sim 400$ km and a pixel granularity of $\Delta\alpha \sim 0.1^\circ$, the pixel size projected on ground is ~ 0.8 km.

6 Some order of magnitude estimates

6.1 Air scintillation signal

Consider a typical hadron-induced EAS with $E = 10^{19}$ eV, at $\gamma = 15^\circ$, with an ideal optics ($\varepsilon'_O[\gamma] = \cos[\gamma]$).

The signal time-integrated irradiance, $d\mathcal{N}/dA$, reaching the apparatus is given in table 6 for different values of θ and H (the other parameter values are the one listed in table 1).

Note the the irradiance scales as $\sim (\cos\gamma/H)^2$.

$d\mathcal{N}/dA \approx [\text{ph}\cdot\text{m}^{-2}]$	$\theta = 30^\circ$	$\theta = 50^\circ$	$\theta = 70^\circ$
$H = 400$ km	40	70	180
$H = 700$ km	15	25	60
$H = 1000$ km	5	10	30

Table 6: Time-integrated irradiance $\frac{d\mathcal{N}}{dA}$ of an EAS.

The detection of such an EAS obviously requires a large entrance pupil of many squared meters (see next section).

The typical angular length and the apparent time duration of the signal are given respectively in table 7 and 8.

$\xi_{\text{EAS}} \approx [^\circ]$	$\theta = 30^\circ$	$\theta = 50^\circ$	$\theta = 70^\circ$
$H = 400$ km	0.8	1.7	3.1
$H = 700$ km	0.4	1.0	1.8
$H = 1000$ km	0.3	0.7	1.2

Table 7: Angular length ξ_{EAS} of an EAS.

$T_{\text{EAS}} \approx [\mu\text{s}]$	$\theta = 30^\circ$	$\theta = 50^\circ$	$\theta = 70^\circ$
$H = 400$ km	60	84	102
$H = 700$ km	60	84	103
$H = 1000$ km	60	84	104

Table 8: Apparent time duration T_{EAS} of an EAS.

6.2 Requirements on the optical triggering efficacy

Following the discussion in section 5.5 we can calculate a required overall photo-detection efficacy in the reference conditions

$$\mathcal{E}_{\text{PD}}(\gamma = 15^\circ) \approx N_{\text{ph}} \left(\frac{d\mathcal{N}}{dA} \right)^{-1},$$

where we remember that $N_{\text{ph}} \simeq 100$. Using the values of the time-integrated irradiance given in the previous section we obtain $\mathcal{E}_{\text{PD}}(\gamma = 15^\circ) \approx 4 \text{ m}^2$ when observing at $H = 700$ km, $\mathcal{E}_{\text{PD}}(\gamma = 15^\circ) \approx 1.5 \text{ m}^2$ at $H = 400$ km and $\mathcal{E}_{\text{PD}}(\gamma = 15^\circ) \approx 10 \text{ m}^2$ at $H = 1000$ km.

If one conservatively assumes a safe overall (including filters, electronics, photo-sensor and filling factor) efficiency $\varepsilon_{\text{PD}} \sim 0.1$, we obtain an optical triggering efficacy, from the (11),

$$\varepsilon'_O(\gamma = 15^\circ) \approx \frac{\mathcal{E}_{\text{PD}}}{\varepsilon_{\text{PD}}} \approx \begin{cases} 15 \text{ m}^2 & \text{at } H = 400 \text{ km} \\ 40 \text{ m}^2 & \text{at } H = 700 \text{ km} \\ 100 \text{ m}^2 & \text{at } H = 1000 \text{ km} \end{cases}. \quad (40)$$

The triggering optical efficacy at $\gamma = 0^\circ$, $A\varepsilon'_O(0^\circ)$, i.e. the entrance pupil area, is not only the effective collection area but it is also an estimate of the physical area of the optics, actually an optimistic one, and consequently a requirement on the minimum size of the telescope.

Translated into minimum area and diameter for the optics we obtain, for an ideal optics in which $\mathcal{E}(\gamma) = S \cos \gamma$,

$$A_{\min} = \mathcal{E}_{\mathcal{O}}^{\text{tri}}(0^\circ) \approx \frac{\mathcal{E}_{\mathcal{O}}^{\text{tri}}(15^\circ)}{\cos 15^\circ} \approx \begin{cases} 16 \text{ m}^2 & \text{at } H = 400 \text{ km} \\ 42 \text{ m}^2 & \text{at } H = 700 \text{ km} \\ 104 \text{ m}^2 & \text{at } H = 1000 \text{ km} \end{cases} \quad (41)$$

$$D_{\min} = 2\sqrt{\frac{A\varepsilon'_{\mathcal{O}}(0^\circ)}{\pi}} \approx \begin{cases} 4.5 \text{ m} & \text{at } H = 400 \text{ km} \\ 7.5 \text{ m} & \text{at } H = 700 \text{ km} \\ 12 \text{ m} & \text{at } H = 1000 \text{ km} \end{cases}$$

This result cannot be applied without accounting for the various sources of inefficiencies in a real optical system. Based on existing designs these inefficiencies can be assumed to reduce the amount of photons in the bucket depending on many factors. Therefore, the previous lower limit on D_{\min} might rise by a factor of $\gg 1$, as confirmed by Monte-Carlo simulations [8, 9, 34, 35].

6.3 Granularity and angular resolution

If we require a spatial granularity on Earth surface $\Delta\ell \lesssim 1 \text{ km}$, we can fix the corresponding pixel granularity at different orbital heights:

$$\Delta\alpha \approx \frac{\Delta\ell}{H} \approx \begin{cases} 0.10^\circ & \text{at } H = 400 \text{ km} \\ 0.06^\circ & \text{at } H = 700 \text{ km} \\ 0.04^\circ & \text{at } H = 1000 \text{ km} \end{cases} \quad (42)$$

Using the values of table 7, one can easily see that at $\theta = 50^\circ$, the EAS is about 17 pixels long; so there are about 6 photons per pixel.

The pixel size on the FS is, from (18), $\delta \approx Df/\# \Delta\ell/H \approx 5 \text{ mm}$, using the minimum diameter given in (41) and a $f/\# \sim 0.5$. The value of δ doesn't depend on H since $D_{\min} \propto H$.

With these numbers one can see that, in the reference conditions, the angular resolution perpendicular and parallel to the line of sight are both $\sim 0.5^\circ$. The total angular resolution is then $\Delta\beta_{\text{tot}} = \sqrt{\Delta\beta_{\perp}^2 + \Delta\beta_{\parallel}^2} \lesssim 1^\circ$.

6.4 The random background (RB)

The total RB rate intercepted on the whole entrance pupil by the apparatus in the reference conditions, with $\gamma_{\text{M}} = 20^\circ$ (corresponding to 0.38 sr full FoV) is given in table 9 together with the corresponding number of pixels and the total RB rate detected per pixel (assuming a total photon efficiency, optics plus photo-detector, $\varepsilon_{\text{T}} \approx 0.1$).

H [km]	N_{pix}	RB_{tot} [THz]	RB_{pix} [MHz]
400	$1.2 \cdot 10^5$	2.8	2.3
700	$3.5 \cdot 10^5$	7.6	2.2
1000	$7.8 \cdot 10^5$	19.0	2.4

Table 9: Number of pixels, total RB rate ($= BA\pi \sin^2[\gamma_{\text{M}}]$) and RB rate per pixel ($= BA\pi \sin^2[\gamma_{\text{M}}] \varepsilon_{\text{T}}/N$). We used the values of A and $\Delta\alpha$ from (41) and (42) respectively.

This gives: one order of magnitude more RB than signal photons superimposed on the typical EAS (all space-time length) and roughly the same number of signal and RB photons near the EAS maximum. The acceptable background level also depends on the energy of the EAS. However to allow for background dependent observations implies a very precise knowledge of the Apparatus sensitivity as a function of the background level.

7 Conclusions

The design of a space-based apparatus for the detection of the EAS produced by UHECP is a challenging task, requiring a careful design and a preparation based on both preliminary studies and measurements and various technological demonstrators.

Some sort of path-finder and/or technology demonstrator is certainly needed.

Acknowledgments

The authors wish to thank the members of the EUSO Collaboration and in particular Osvaldo Catalano (INAF/IASF-Palermo), Lloyd Hillman (University of Alabama Huntsville) deceased, Didier Lebrun (LPSC, Grenoble), Piero Mazzinghi (INOA, Firenze) and Sergio Bottai (INFN, Firenze) for many useful discussions and suggestions.

The pioneering work [7] of Katsushi Arisaka (UCLA, Los Angeles) is acknowledged.

References

- [1] J. Abraham et al. *Phys. Rev. Lett.*, 101:061101, 2008. arXiv: 0806.4302 [astro-ph].
- [2] S. Westerhoff. *Experimental ultra-high-energy cosmic ray physics*. hep-ex/0512018, 2005.
- [3] A. A. Watson. *Observations of ultra-high energy cosmic rays*. astro-ph/0511800, 2005.
- [4] S. Petrerá. Ultra High Energy Cosmic Rays from earth-based observatories. 2008. arXiv: 0810.4710 [astro-ph].
- [5] A. A. Watson. *Nucl. Instrum. Meth.*, A588:221–226, 2008.
- [6] J. Abraham et al. *Astropart. Phys.*, 29:188–204, 2008. arXiv: 0712.2843 [astro-ph].
- [7] K. Arisaka. *Optimization of an OWL-Airwatch Optics and Photo-Detectors*, December 1999.
- [8] A. Thea et al. *Proc. 29th ICRC*. volume 8, pages 129–132, 2005.
- [9] A. Thea et al. *Proc. 29th ICRC*. volume 8, pages 133–136, 2005.
- [10] J. Adams. *Nucl. Phys. Proc. Suppl.*, 134:15–22, 2004.
- [11] T. Ebisuzaki et al. *Nucl. Phys. Proc. Suppl.*, 175-176:237–240, 2008.
- [12] A. Santangelo, A. Petrolini, et al. *S-EUSO: a proposal for a space-based observatory for UHECP*. Technical report, 2007. www.ge.infn.it/euso/docs/S-EUSO_Proposal.pdf.
- [13] ESA. *Cosmic Vision. Space Science for Europe 2015-2025*, 2005.
- [14] The EUSO Collaboration. *EUSO: Report on the Phase A Study*, 2003. Internal note EUSO-PI-REP-002.
- [15] J. Linsley. *Call for project and ideas in High Energy Astrophysics*, 1979.
- [16] Orbiting Wide-angle Light-collectors <http://owl.gsfc.nasa.gov/>.
- [17] V. I. Abrashkin et al. *Int. J. Mod. Phys.*, A20:6865–6868, 2005.
- [18] A. N. Cox, editor. *Allen’s Astrophysical Quantities*. AIP Press, 1999.
- [19] We were not able to find official references related with Linsley’s standard atmosphere model. References [45, 46] contain informations about parametrization data.
- [20] US Standard Atmosphere http://modelweb.gsfc.nasa.gov/atmos/us_standard.html.
- [21] T. K. Gaisser and A. M. Hillas. *Proc. 15th ICRC*, 8, 353. 1977.
- [22] C. Pryke. *Astropart. Phys.*, 14:319–328, 2001. astro-ph/0003442.
- [23] T. Stanev. *High Energy Cosmic Rays*. Springer, 2004.
- [24] F. Kakimoto et al. *Nucl. Instrum. Meth.*, A372:527–533, 1996.
- [25] M. Nagano and K. others. *Astropart. Phys.*, 22:235–248, 2004. arXiv: astro-ph/0406474.
- [26] A. Bucholtz. *Applied Optics*, 34(15):2765–2773, 1995.
- [27] A. T. Young. *Applied Optics*, 33(6):1108–1110, 1994.

- [28] L. W. Hillman. *Private communications*, 2004.
- [29] P. Sommers. *Astropart. Phys.*, 3:349–360, 1995.
- [30] R. M. Baltrusaitis et al. *Nucl. Instrum. Meth.*, A240:410–428, 1985.
- [31] A. Piccioli et al. *Nucl. Instrum. Meth.*, A504:294–297, 2003.
- [32] P. Buzhan et al. *Nucl. Instrum. Meth.*, A504:48–52, 2003.
- [33] V. Golovin and V. Savelev. *Nucl. Instrum. Meth.*, A518:560–564, 2004.
- [34] A. Thea. *Observation of UHECR from space*. PhD thesis, Università degli Studi di Genova, 2006. www.ge.infn.it/euso/docs/AThea_PhDThesis.pdf.
- [35] R. Pesce. *The observation of UHECP on the Earth and from space*. PhD thesis, Università degli Studi di Genova, 2008. www.ge.infn.it/euso/docs/RPesce_PhDThesis.pdf.
- [36] J. Wertz and W. Larson, editors. *Space missions analysis and design*. Microcosm Press, 1999.
- [37] P. Mazzinghi et al. *Physics and Astrophysics in Space*, Frascati Physics Series vol. xxxvii, 437-444. 2004.
- [38] C. Berat et al. The light of the night sky in euso: Duty cycle and background. Prepared for 28th International Cosmic Ray Conferences (ICRC 2003), Tsukuba, Japan, 31 Jul - 7 Aug 2003.
- [39] O. Catalano et al. *Nucl. Instr. Methods A*, 480(2-3):547–554, 2002.
- [40] L. M. Barbier et al. *Astropart. Phys.*, 22:439–449, 2005.
- [41] D. J. Knecht et al. *Advances in Space Research*, 19(4):627–630, 1997.
- [42] G. K. Garipov et al. *JEPT Letters*, 82(4):185–187, 2005.
- [43] A. Thea et al. *Nucl. Phys. B Proc. Suppl.*, 166:223–228, 2006.
- [44] International Satellite Cloud Climatology Project <http://isccp.giss.nasa.gov/>.
- [45] D. Heck et al. *CORSIKA: A Monte Carlo code to simulate Extensive Air Showers*. www-ik.fzk.de/corsika/.
- [46] B. Keilhauer et al. *Astropart. Phys.*, 25:259–268, 2006. arXiv: astro-ph/0511153.
- [47] G. W. Snedecor and W. G. Cochran. *Statistical methods*. Iowa State University Press, 1967.